國 立 交 通 大 學

電子工程學系電子研究所

碩 士 論 文

二氧化矽薄膜所誘發之選擇性混合效應
對砷化銦鎵量子井之影響

Studies of SiO_2-Induced Selective Disordering
of InGaAs/GaAs Quantum Wells

研 究 生： 陳 雅 婷

指導教授： 李 建 平 博士

中 華 民 國 九十九 年 六 月

二氧化矽薄膜所誘發之選擇性混合效應對砷化銦鎵量子井之影響

Studies of SiO_2-Induced Selective Disordering of InGaAs/GaAs Quantum Wells

研 究 生：陳雅婷　　Student：Ya-Ting Chen

指導教授：李建平 博士　　Adviser：Dr. Chien-Ping Lee

國 立 交 通 大 學

電子工程學系　電子研究所

碩 士 論 文

A Thesis
Submitted to Department of Electronics Engineering
Institute of Electronics
College of Electrical and Computer Engineering
National Chiao Tung University
in Partial Fulfillment of the Requirements
for the degree of
Master
in
Electronics Engineering

June 2010

Hsinchu, Taiwan, Republic of China

中華民國九十九年六月

二氧化矽薄膜所誘發之選擇性混合效應對砷化銦鎵量子井之影響

學生：陳雅婷　　　　　　　　　　　　　　　　　　指導教授：李建平 博士

國立交通大學

電子工程學系 電子研究所碩士班

摘　　要

本論文致力於研究介電薄膜所誘發之選擇性量子井混合效應。我們將砷化銦鎵量子井異質結構之樣品，鍍上二氧化矽或二氧化鈦薄膜，利用高溫快速熱退火引發量子井混合效應，並量測低溫之激發光譜，以探討其光學性質。經由 900 ℃ 高溫快速熱退火之處理，二氧化矽薄膜能增強砷化銦鎵量子井之混合效應，其能量藍移現象可高達 100 meV；相對之下，二氧化鈦薄膜對於砷化銦鎵量子井之混合效應展現抑制的效果，產生 9.5 meV 之能量紅移現象。此外，我們更在二氧化矽薄膜上設計次微米大小之圓形圖樣，藉以誘發部分選擇性量子井混合。圖樣之大小與激發光源之強度，皆會影響部分選擇性量子井混合效應，並可由其對應之低溫激發光譜觀察出趨勢。我們推論，在每個退火溫度條件下，皆有其相對應之特定最小有效直徑；並從能量空間及實際空間的觀點分析電子分佈，進一步解讀不同激發光源強度下之低溫激發光譜。

Studies of SiO_2-Induced Selective Disordering of InGaAs/GaAs Quantum Wells

Student: Ya-Ting Chen Advisor: Dr. Chien-Ping Lee

Department of Electronics Engineering and Institute of Electronics

National Chiao Tung University

Abstract

In this thesis, we aimed at investigating the selective area quantum well intermixing induced by dielectric capping layers. The $InGaAs/GaAs$ quantum well heterostructures were capped with SiO_2 and TiO_2 films, and high-temperature rapid thermal annealing was applied subsequently. The optical properties were examined by measuring photoluminescence and micro-photoluminescence spectra at 77 K. When the rapid thermal annealing was processed at 900 ℃, an energy blue-shift as large as 100 meV was observed from the SiO_2-enhanced quantum well intermixing, and a meaningful energy red-shift of 9.25 meV was offered with the help of TiO_2 as an inhibitor of the thermal-induced atomic interdiffusion. Furthermore, the patterns with circular apertures which are sub-micrometer in diameter were fabricated on the SiO_2 capping layers as masks. From the aperture-dependent micro-PL spectra, we suggest that the minimum effective diameter of apertures is limited to a specific value for each RTA temperature. We also demonstrated the distribution of electrons from the points of view both in the real space and in the energy space so as to explain the excitation power-dependent transformation of emission peaks. The controllable selective area InGaAs/GaAs quantum well intermixing was successfully accomplished on the sub-micrometer scale with the assistance of patterned SiO_2 capping layer, and this would pave a way to realize the monolithic integration of optoelectronic devices.

Acknowledgements

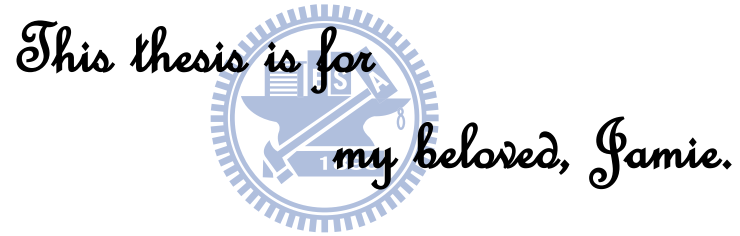

Contents

ABSTRACT (Chinese) ………………………………………………………..…. i

ABSTRACT (English) ………………………………………………………..…. ii

ACKNOWLEDGEMENTS ……………………………………………………. iii

CONTENTS …………………………………………………………………….…. iv

NOTATIONS ……………………………………………………………………. vi

CHAPTER 1 INTRODUCTION

1.1 Selective Area Quantum Well Intermixing ……………………………………... 1

1.2 Previous Studies ....…………………………………………………………………… 2

1.3 Our Approaches and What We Have Done

1.3.1 Dielectric Capping Film Induced Selective Interdiffusion ………………...... 3

1.3.2 Selective Quantum Well Intermixing on the Submicron Scale …………….... 4

CHAPTER 2 MECHANISM FOR SiO_2 ENHANCED INTERMIXING AND ITS INFLUENCE ON ENERGY BAND PROFILE

2.1 Vacancy-Assisted InGaAs/GaAs Quantum Well Intermixing

2.1.1 Diffusion Mechanism …………………………………………………...…. 5

2.1.2 Vacancy-Enhanced Quantum Well Interdiffusion …………………………… 7

2.1.3 SiO_2-Induced InGaAs/GaAs Quantum Well Interdiffusion

2.1.3.1 Vacancy Generation via Thermal Treatment ………………………….. 8

2.1.3.2 Strain-Dependent Vacancy Distribution ……………………………..… 10

2.1.3.3 Vacancy-Assisted In-Ga Interdiffusion ………………………...…… 12

2.2 Band Profile Modification via In Atom Diffusion ……………………..……… 14

CHAPTER 3 RESULTS AND DISSCUSSION

3.1 Capping Layer-Induced Energy Shift via Thermal Treatment

3.1.1 Influence of SiO_2 Capping Layer ……………………………………..… 17

3.1.2 Influence of TiO_2 Capping Layer …………………………...…………… 21

3.2 Selective Quantum Well Intermixing via Patterned SiO_2 Layer

3.2.1 Spatial Resolution of Micro-Photoluminescence ………………………..… 26

3.2.2 Aperture Size-Dependent Energy Shift ………………………………..…… 30

3.2.3 Excitation Power-Dependent Emission Wavelength ……………………..…… 37

CHAPTER 4 CONCLUSIONS …………………………………………..……… 46

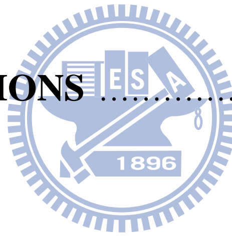

REFERENCE …………………………………………………………………… 47

APPENDIX ……………………………………………………………………… 49

VITA …………………………………………………………………………… 56

Notations

a, a_c, a_v	Hydrostatic deformation potential		eV
a_{sub}, a_{epi}	Lattice Constant		$\dot{A}$
b	Shear deformation potential		eV
e	Electronic charge	$1.602176487 \times 10^{-19}$	C
$\hbar$	Reduced Plank Constant	6.582119×10^{-16}	$eV \cdot s$
j	Flux in diffusion equations		
k_B	Boltzmann constant	8.617343×10^{-5}	eV/K
m_0	Free electron mass	9.109382×10^{-31}	kg
m^*, m_e, m_h	Effective mass		kg
t	Time		sec
w	Width		m
C	Concentration in diffusion equations		
C_{11}, C_{12}	Elastic Stiffness		$\times 10^{11}\ dyn/cm^2$
C_Γ	Bowing parameter	0.477	eV
D, D_0	Diffusion coefficient or Diffusivity		m^2/K
E	Energy		eV
E_A	Activation energy		eV

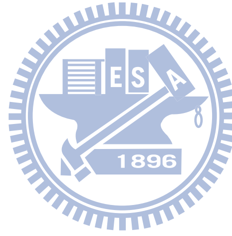

$\Delta \boldsymbol{E}$	Energy shift	eV
$\boldsymbol{H}$	Hydrostatic-pressure induced energy shift	eV
$\boldsymbol{L_D}$	Diffusion length	m
$\boldsymbol{S}$	Strain Potential Energy	eV
$\boldsymbol{T}$	Temperature	℃ or K
$\boldsymbol{V}, \boldsymbol{V_c}, \boldsymbol{V_v}$	Potential Energy	eV
$\boldsymbol{\alpha}$	Thermal expansion coefficient	$\times 10^{-6}$ ℃$^{-1}$
$\boldsymbol{\varepsilon}$	Strain	
$\boldsymbol{\delta}$	Biaxial stress-induced valence band splitting	eV
$\boldsymbol{\phi}$	Density in diffusion equations	
$\boldsymbol{\varphi}$	Wave function in Schrödinger equation	
$\boldsymbol{\chi_i}, \boldsymbol{\chi_o}$	Composition of In atoms	

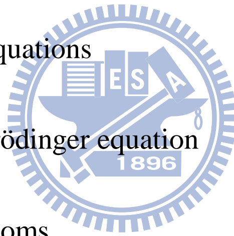

Chapter 1

Introduction

1.1 Selective Area Quantum Well Intermixing

In recent years, Quantum-confined heterostructures, such as quantum wells (QWs) and quantum dots (QDs), have come into great notice, since their potential applications leading to significant improvements for the optoelectronic and photonic devices are expected [1-3]. QWs/QDs intermixing, also known as interdiffusion or disordering, has been one of the commonest band gap tuning techniques [4]. Band gap tuning is of great importance because the corresponding optical properties, such as absorption spectrum and refractive index, have crucial influence on the performance of devices.

Selective area quantum well intermixing is especially useful for the fabrication of monolithic integrated semiconductor devices, such as QW lasers, photodetectors, modulators and passive waveguides. When intermixing is stimulated only in selected areas of a sample, permanent lateral barriers can be built inside the quantum well. Accordingly, several localized regions of different effective energy band gap can be laterally integrated within the same epitaxy structures simultaneously. On the whole, selective interdiffusion offers a promising candidate for considerable advantages to better improve the integration of optoelectronic and photonic devices.

1.2 Previous Studies

There are two major approaches which can establish precise control over spatial interdiffusion. Selective area epitaxy is conventionally utilized [5, 6], while post-growth techniques provide a relatively simpler and cost-effective method and thus are regarded as promising alternatives [7, 8]. Post-growth band gap tuning techniques can be classified into two main categories: impurity-induced layer disordering (IILD) and impurity-free vacancy disordering (IFVD). Extensive investigations into impurity-induced layer disordering, such as ion-implantation-induced intermixing, in the lattice-matched $GaA/AlGaAs$ QW systems have been reported [9, 10]. Meanwhile, impurity-free vacancy disordering has also attracted considerable interest as it causes no excess residual damages which are regarded as one of the main factors in deteriorating the device performance and reliability.

One of the IFVD techniques generally adopted is laser-beam-induced disordering which offers the possibility of being impurity-free and direct write capability [11, 12]. However, it concurrently induces thermal shock during the material melting process which uses a pulse mode with high power density and thus results in potentially undesirable redistribution of dopants outside the active region of devices.

In contrast, dielectric layer encapsulation technique has long been used to provide a milder and more harmless method to control interdiffusion processes [13]. The surface of QW samples has been capped with a variety of dielectric layers, such as silicon dioxide (SiO_2) [14, 15] , titanium dioxide (TiO_2) [16, 17], silicon nitride (Si_3N_4) [18, 19], and strontium fluoride (SrF_2) [20]. After the deposition process, subsequent thermal treatment or annealing is then applied to initialize the atomic interdiffusion.

1.3 Our Approaches and What We Have Done

Even though impurity-free vacancy disordering (IFVD) has been studied in many aspects, little research has been devoted to the topic of photon-confinement via spatially selective area interdiffusion. The intention of our work was to demonstrate a feasible method to fabricate artificial quantum structures with proper physical properties in the designed selective area, while self-assembled QDs are commonly formed in the unexpected area. This selective area interdiffusion technique will provide a promising candidate for enormous advantages to better improve the monolithic integration of optoelectronic devices.

1.3.1 Dielectric Capping Film Induced Selective Interdiffusion

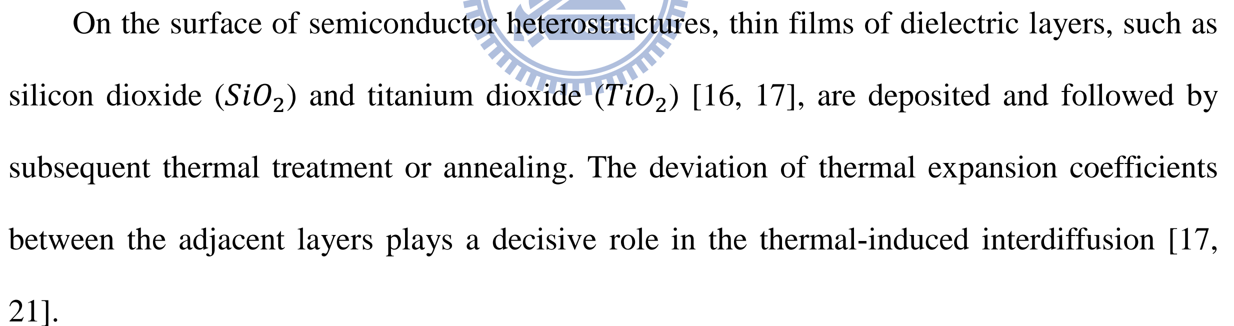

On the surface of semiconductor heterostructures, thin films of dielectric layers, such as silicon dioxide (SiO_2) and titanium dioxide (TiO_2) [16, 17], are deposited and followed by subsequent thermal treatment or annealing. The deviation of thermal expansion coefficients between the adjacent layers plays a decisive role in the thermal-induced interdiffusion [17, 21].

During the annealing process, either compressive or tensile strain is created in the semiconductor layers. Provided that SiO_2 with a comparatively smaller thermal expansion coefficient serves as the capping layer, compressive strain and group III vacancies are created in the underlying $GaAs$-based quantum structures during the annealing process. With the help with compressive strain field, the generated group III vacancies diffuse downwards to the quantum well layers and serve as a driving force in the interdiffusion of group III atoms. As a result, SiO_2-enhanced atomic interdiffusion can be put into practice.

On the contrary, tensile strain is created instead and group III vacancies are unlikely to

be generated when the $GaAs$-based heterostructures are capped with TiO_2, of which the thermal expansion coefficient is comparatively larger. In this case, TiO_2 behaves as an inhibitor of the atomic interdiffusion.

In brief, the compositions, shapes, and dimensions of QWs/QDs can be modified by the thermal-induced atomic interdiffusion, and thus the corresponding optical and electrical properties are able to be tuned as well.

1.3.2 Selective Quantum Well Intermixing on the Submicron Scale

For the purpose of selective area wavelength tuning of $InGaAs/GaAs$ quantum well, capping layers are patterned to function as masks. The patterned SiO_2 capping layer not only builds in-plane (xy plane) lateral potential but also establishes vertical potential by inducing the atomic interdiffusion along the growth-direction (z-direction). Hence, a three-dimensional (3D) confined potential is able to be created by selective area quantum well intermixing.

It is known that semiconductor properties can be quite different when the scale is down to nano-meter. In this study, we designed circular apertures for the patterns which are sub-micrometer in diameter (d = 55, 75, 100, 125, 135 nm) and examine the corresponding optical properties by means of micro-photoluminescence (micro-PL) measurement.

Chapter 2

Mechanism for SiO_2 Enhanced Intermixing and Its Influence on Energy Band Profile

2.1 Vacancy-Assisted InGaAs/GaAs Quantum Well Intermixing

The atomic diffusion may be dominated by either interstitials or vacancies according to their distinguishable diffusion coefficients. In the $InGaAs/GaAs$ quantum well systems we used, Group III vacancies govern the atomic interdiffusion

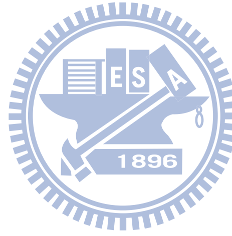

2.1.1 Diffusion Mechanism

The kinetics of compositional disordering in the $In_{\chi_i}Ga_{(1-\chi_i)}As/GaAs$ quantum well systems can be perfectly illustrated by the conventional diffusion model.

The diffusion equation is derived from the continuity equation, which describes the transport of a conserved quantity in a system. In the system, no material is effectively created or destroyed, namely to obey the conservation law. Inflow and outflow of the diffusing material lead to a change in density in any part of the system.

$$\frac{\partial \phi(r,t)}{\partial t} + \nabla \cdot j = 0 \qquad (1)$$

where $\phi(r,t)$ is the density at location r and time t, and j is the flux of the diffusing material.

$$j = -D(\phi)\nabla\phi(r,t) \qquad (2)$$

According to Fick's first law, the flux j is proportional to the local density gradient $\nabla\phi(r,t)$, and $D(\phi)$ is the diffusion coefficient, or called diffusivity.

If D is a constant independent of the density and coordinate, Fick's second law yields the linear equation shown below.

$$\frac{\partial\phi(r,t)}{\partial t} = D\nabla^2\phi(r,t) \tag{3}$$

The $In_{\chi_i}Ga_{(1-\chi_i)}As/GaAs$ quantum well structures in our experiments have isotropic properties in the x-direction and y-direction and can be reasonably assumed to be identical. Hence, the diffusion model can be demonstrated by the following simplified one-dimensional diffusion equation in x-direction.

$$\frac{\partial}{\partial t}C(x,t) = D\,\frac{\partial^2}{\partial x^2}C(x,t) \tag{4}$$

In Eq. (4), $C(x,t)$ is the concentration of material, and D is its diffusivity. The concentration of In (C_{In}) also indicates the In composition (χ_i) in the $In_{\chi_i}Ga_{(1-\chi_i)}As$ quantum well, and the diffusion equation we used can also be expressed in the χ_i form.

$$\frac{\partial}{\partial t}\chi_i(x,t) = D_{In-Ga}(T)\,\frac{\partial^2}{\partial x^2}\chi_i(x,t) \tag{5}$$

Owing to the different In composition in the barriers from that in the well, the In composition gradient ($\nabla\chi_i$) serves as a driving force in the diffusion mechanism. In Eq. (5), D_{In-Ga} is the intrinsic diffusivity of the $In-Ga$ interdiffusion, which is a parameter obtained from the experimental results. The diffusion coefficient in solids is found to be well predicted as a function of temperature (T) and activation energy (E_A).

$$D(T) = D_0 \cdot e^{\frac{-E_A}{k_B T}} \tag{6}$$

where D_0 is the maximum diffusion coefficient at infinite temperature.

The composition profile as a function of diffusion length ($L_D = \sqrt{Dt}$) can be calculated by using the solution of error function.

$$\chi_i(x) = \frac{1}{2}\chi_o \left[erf\left(\frac{\frac{w}{2}-x}{2L_D}\right) + erf\left(\frac{\frac{w}{2}+x}{2L_D}\right) \right] \quad (7)$$

where χ_o is the In composition within the well before interdiffusion starts while the $In_{\chi_0}Ga_{(1-\chi_0)}As$ well is centered at $x = 0$ and ranged from $x = \frac{-w}{2}$ to $x = \frac{+w}{2}$.

Fig. 2.1 illustrates the L_D-dependent In composition profile. We used the computing software, named “MATLAB”, to simulate the condition of $\chi_o = 0.22$.

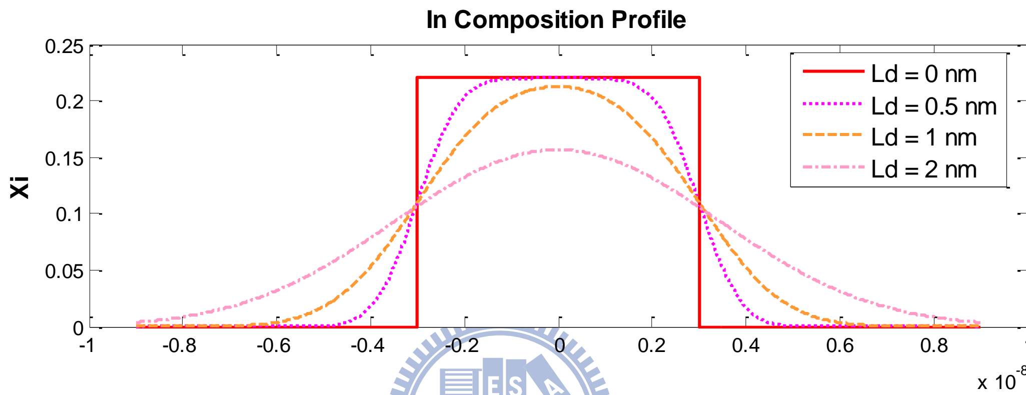

Fig. 2.1 In composition profile with different diffusion length (L_D= 0, 0.5, 1, 2 nm) under the condition of $\chi_o = 0.22$. (This profile is the results of simulation by using the computing software, “MATLAB”.)

2.1.2 Vacancy-Enhanced Quantum Well Interdiffusion

The atomic diffusion may be governed by either interstitials or vacancies according to their distinguishable diffusion coefficients. In this thesis, Group III vacancies-dominated interdiffusion is demonstrated via taking impurity-free vacancy disordering (IFVD) as an example.

V_{III}-dominated impurity-free vacancy disordering (IFVD) is found to be a two-step mechanism, including the creation of group III vacancies (V_{III}) by out-diffusion of group

III atoms from the semiconductor layer into the dielectric capping layer and the following diffusion of V_{III} away from the dielectric film-semiconductor interface. The first step is activated by high temperature thermal treatment which leads to the thermal expansion mismatch between two adjacent layers. The V_{III} generated at the interface subsequently penetrate into the underlying layers and enhance the redistribution of group III atoms in the quantum well structure. As a result, the band gap profile of the semiconductor is altered.

2.1.3 SiO$_2$-Induced InGaAs/GaAs Quantum Well Interdiffusion

SiO_2 is an ideal candidate for the modification of optoelectronic properties in $GaAs$-based structures. The $InGaAs/GaAs$ quantum well structure capped with SiO_2 dielectric film on the surface is investigated in this study.

The $In_{\chi_i}Ga_{(1-\chi_i)}As/GaAs$ quantum wells in our experiments are grown along $(0\ 0\ 1)$ direction, also called z-direction in this thesis, on $(0\ 0\ 1)$ $GaAs$ substrate. Two assumptions are made to simply the diffusion model. First, the stress along the growth direction is completely released during the epitaxy process, and no stress along z-direction is considered. Second, the in-plane x-direction and y-direction are identical to produce a tetrahedral distortion.

2.1.3.1 Vacancy Generation via Thermal Treatment

Two possible factors dominate the generation of excess vacancies (V_{Ga}) at the SiO_2-$GaAs$ interface. One is the solubility of Ga atoms in the SiO_2 capping layer, and the other comes from the difference of the thermal expansion coefficients of SiO_2 and $GaAs$.

The generation of V_{Ga} is also under the control of the dielectric film quality depending on deposition conditions and the film thickness which controls the number of Ga atoms that can be absorbed into the layer, yet these minor influential factors are not discussed here.

The distinctive affinity of SiO_2 for Ga atoms makes it behave as a perfect solvent and absorb Ga preferentially rather than As atoms. In other words, SiO_2 could be seen as a Ga sink source or a sponge that rapidly absorbs Ga atoms up to its solubility limit.

High temperature thermal treatments are applied after the deposition of capping layer so as to build a thermal strain field which mainly results from the significantly smaller thermal expansion coefficient of $GaAs$ than SiO_2. The thermal expansion coefficient measures the fractional change in size of an object per degree change in temperature and can be written as Eq. (8).

$$\alpha = \frac{1}{V}\frac{dV}{dT} \tag{8}$$

If the thermal expansion coefficient is not a variable of temperature in the range of temperature we considered, the fractional change in volume can be calculated by the following equation.

$$\frac{\Delta V}{V} = \alpha \Delta T \tag{9}$$

Thermal expansion coefficients of the materials used in our experiment are listed in Table 2.1. The obvious difference of thermal expansion coefficients can be found between $GaAs$ and SiO_2 while the thermal expansion coefficients of $GaAs$ and $InGaAs$ can assumed to be identical.

After high temperature annealing, the semiconductor layers of $GaAs$ and $InGaAs$ experience compressive strain in comparison with the tensile strain in the SiO_2 capping layer. The compressive strain in the $GaAs$ layer tends to eject vacancy defects and therefore aid the movement of V_{Ga} to penetrate into the underlying $InGaAs$ quantum well structure. The closer to the SiO_2-$GaAs$ interface, the more serious the compressive strain is. The

spontaneously created compressive strain gradient in the $GaAs$ layer ensures V_{Ga} diffuse smoothly toward the $InGaAs$ quantum well.

Table 2.1 Thermal Expansion Coefficients [16]

Material	Thermal Expansion Coefficient α ($\times 10^{-6}$ °C^{-1})
SiO_2	0.52
TiO_2	8.2
$GaAs$	6.03
$InGaAs$	5.07

In brief, the SiO_2 capping layer attracts Ga atoms to out-diffuse from the adjacent $GaAs$ layer, and meanwhile the remaining Ga vacancies (V_{Ga}) in the $GaAs$ layer diffuse in the opposite direction with the help of the compressive stress field. The Ga vacancies (V_{Ga}) diffused to the $InGaAs/GaAs$ quantum well make substantial contribution to the $In-Ga$ interdiffusion, and the vacancy-assisted interdiffusion mechanism will be discussed later in Section 2.1.3.3.

2.1.3.2 Strain-Dependent Vacancy Distribution

The SiO_2 capping layer can also play the role of patterning mask which is designed for specific apertures with various diameters. It is known that the heterostructures with dielectric capping layers behave quite distinctly from those without capping layers. The patterned samples, hence, display a two-dimensional strain profile which is in strong relation to the scheme of patterns.

The excess Ga vacancies (V_{Ga}) created under the SiO_2-$GaAs$ interface are therefore drained toward the higher compressive regions located under the SiO_2 layer while the adjacent strongly tensile regions located under the apertures act as barriers to this vacancy diffusion. More importantly, extremely high strain on the boundary of patterns can provide a better confinement of V_{Ga} in the region under the SiO_2 layer. In Consequence, this stress-driven anisotropic diffusion in the z-direction can lead to high lateral resolution of the selective area quantum well intermixing.

Figure 2.2 shows the cross-sectional strain profile in the $InAs/GaAs$ quantum dot structures capped with SiO_2/TiO_2 layers [16]. SiO_2 and TiO_2 capping layers respectively contribute to compressive and tensile strain in the semiconductor layers. Also, extremely high strain is observed under the boundary of patterns.

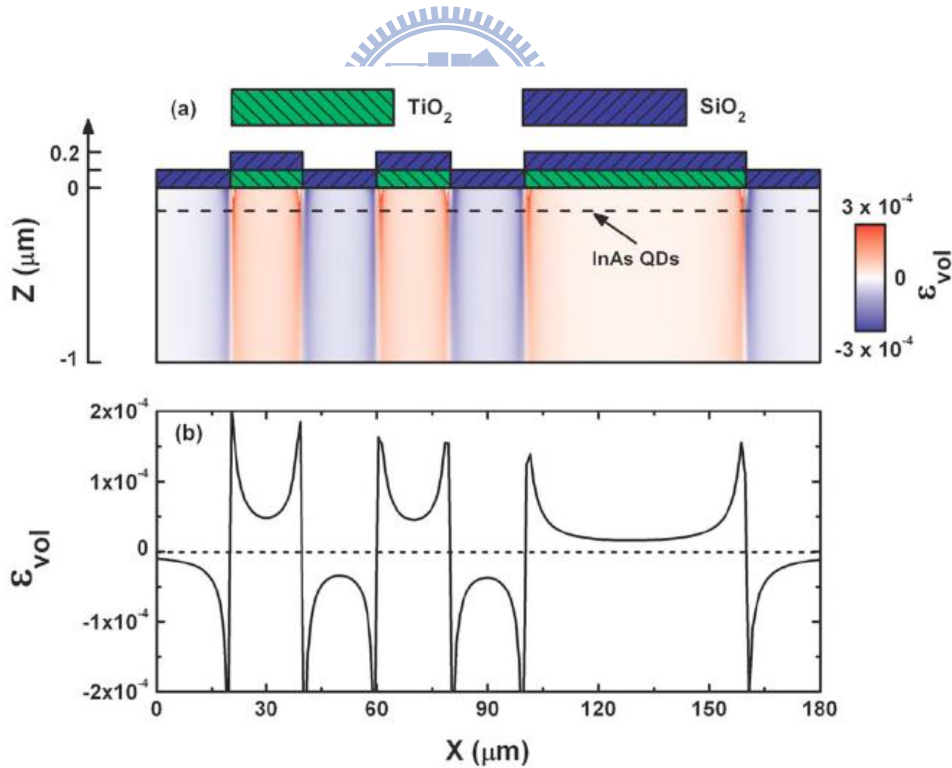

Fig. 2.2 The cross-sectional profile of strain distribution under the patterning SiO_2 and TiO_2 capping layers [16]

The V_{Ga} distribution may perfectly comply with the profile of strain field and is schematically presented in figure 2.3. The Ga vacancies (V_{Ga}) accumulate near the SiO_2-$GaAs$ interface in the beginning of the diffusion process, and then diffuse downward the underlying layers. Because of the barrier formed by the drastic strain variation, very few V_{Ga} will diffuse through the boundary and toward the region without SiO_2 capping layers. Theoretically, we don't have to take into account the slight influence of the vacancy-enhanced intermixing phenomenon in the uncapped area when the lateral diffusion is minor.

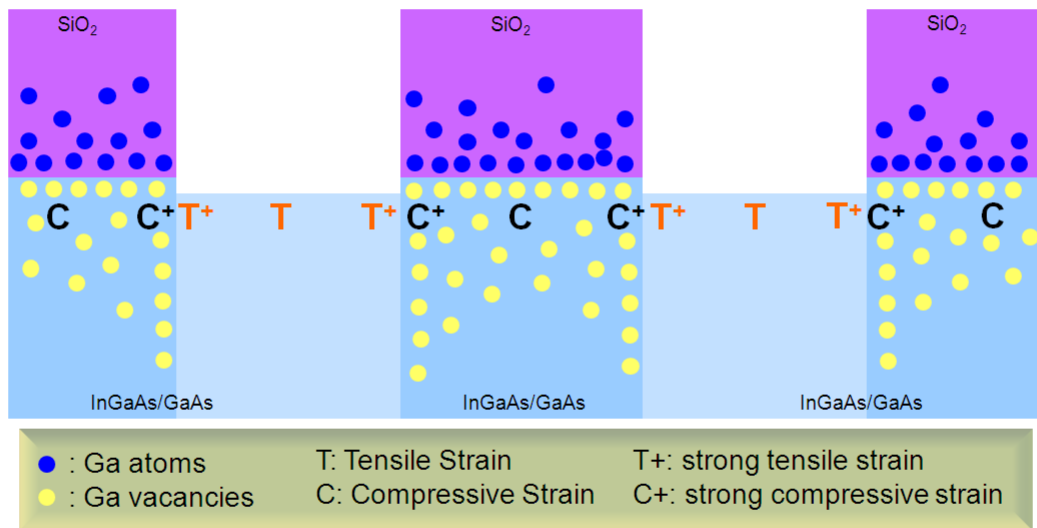

Fig. 2.3 Schematic cross-sectional view of V_{Ga} distribution obeying the strain profile

2.1.3.3 Vacancy-Assisted In-Ga Interdiffusion

In the $InGaAs/GaAs$ quantum well systems, Group III-governed interdiffusion mechanism describes the movement of the diffusing components. The Ga vacancies (V_{Ga}) generated in the top $GaAs$ layer play an important role in the diffusion of In atoms. The existing Ga vacancies reserve the position for the diffusing In atoms so as to significantly

enhance the In diffusion process. Thus, the V_{Ga} movement should also be taken into consideration when the $InGaAs/GaAs$ quantum well intermixing is estimated. The compositional disordering of In concentration is written as the following diffusion equation.

$$\frac{\partial}{\partial t}C_{In}(x,t) = \frac{\partial}{\partial x}\left(C_v'(x,T)D_{In-Ga}(T)\frac{\partial}{\partial x}C_{In}(x,t)\right) \qquad (10)$$

where D_{In-Ga} stands for the intrinsic diffusivity of In-Ga interdiffusion. C_v' is defined as the ratio of V_{Ga} concentration and $C_{v,eq}$ is the equilibrium vacancy concentration dependent on the annealing temperature.

$$C_v'(x,t) = \frac{C_v(x,t)}{C_{v,eq}(T)} \qquad (11)$$

Ga vacancies travel throughout the samples in the manner of diffusion.

$$\frac{\partial}{\partial t}C_v'(x,t) = D_v(T)\frac{\partial^2}{\partial x^2}C_v'(x,t) \qquad (12)$$

where D_v is the diffusivity of Ga vacancies and assumed to be constant independent of In composition.

It is known that the effective diffusion coefficient (D_{eff}) for the interdiffusion is the product of the concentration of the diffusing point defects, which indicate Ga vacancies here, and their diffusivity.

$$D_{eff} = C_v'(x,t)D_{In-Ga}(T) \qquad (13)$$

The vacancy-enhanced diffusivity of In - Ga interdiffusion, or the effective interdiffusion diffusivity (D_{eff}), has been found to be two orders of magnitude higher than that of intrinsic In-Ga interdiffusion [22].

2.2 Band Profile Modification via In Atom Diffusion

The energy band profiles dependent on In composition (χ_i) and the corresponding quantized energy levels after intermixing are acquired by solving the diffusion equation and the Schrödinger equation numerically. On the assumption that In diffusion obeys Fick's second law, the post-annealed In composition (χ_i) distribution can be simply expressed as error-function forms. Composition-dependent properties, such as effective mass, energy band gap, and stress-related coefficients, can be directly derived. Since all the parameters needed are determined, then the Schrödinger equation is possible to be solved.

In quantum mechanics, the Schrödinger equation describes how the quantum state of a physical system changes in time.

$$i\hbar\frac{\partial\Psi}{\partial t}=\left(-\frac{\hbar^2}{2m}\nabla^2+V\right)\Psi \tag{14}$$

Assuming that the potential energy is invariable in time, Schrödinger equation can be simplified to the time-independent Schrödinger equation by the method of separation of variables. Approximate solutions to the time-independent Schrödinger equation are commonly used to calculate the energy levels and other properties of atoms and molecules. In a crystal, the wave function of an electron with energy E in the conduction or valence bands can be estimated by solving the following equation.

$$\left(\frac{-\hbar^2}{2m^*}\nabla^2+V(r)\right)\varphi=E \tag{15}$$

where φ is the wave function of the electron with effective mass (m^*), and $V(r)$ is the potential of the crystal lattice seen by the electron.

In the strained $InGaAs/GaAs$ systems, lattice-mismatch induced strain potential energy (S) cannot be ignored when considering the potential terms in the Schrödinger equation. Actually, the Schrödinger equation is written as a more accurate form as Eq. (16)

$$\left(\frac{-\hbar^2}{2m^*}\frac{\partial^2}{\partial x^2}+V+S\right)\varphi=E\varphi \tag{16}$$

The $In_{\chi_i}Ga_{(1-\chi_i)}As/GaAs$ heterostructure form a lattice-mismatched system because the lattice constant of bulk $In_{\chi_i}Ga_{(1-\chi_i)}As$ is significantly larger than the lattice constant of bulk $GaAs$. Built-in biaxial elastic stress is generated when the pseudomorphic $In_{\chi_i}Ga_{(1-\chi_i)}As$ layer is grown on $GaAs$ substrate. The biaxial stress in the xy plane comes up with the result of hydrostatic deformation and shear deformation. The strain potential energy (S) can be analyzed as a combination of hydrostatic stress induced energy shift (H) and shear stress induced valence band splitting energy (δ).

$$S = H(a) + \delta(b) \tag{17}$$

where a and b stand for the hydrostatic deformation potential and the shear deformation potential respectively.

The hydrostatic stress influences both conduction band and valence band while only valence band is affected by the shear deformation potential which causes heavy-hole (HH) and light-hole (LH) splitting. The strain potential energy (S) is also decided by the value of ε and the elastic constants (C_{ij}). The corresponding strain potential energies for conduction band (S_c) and valence band (S_v) are shown in the following relations.

$$S_c = H(a_c) = 2a_c \frac{C_{11}-C_{12}}{C_{11}} \varepsilon \tag{18}$$

$$S_v = H(a_v) + \delta(b) = \left(2a_v \frac{C_{11}-C_{12}}{C_{11}} \pm b \frac{C_{11}+2C_{12}}{C_{11}}\right) \cdot \varepsilon \qquad \pm: for \ {}^{HH}_{LH} \tag{19}$$

where $a_{c,v}$ is the hydrostatic deformation potential, and b is the shear deformation potential. C_{11} and C_{12} are the elastic stiffness constants. Strain of the epitaxial layer (ε) is defined in Eq. (20). All the strain-related constants, including $a_{c,v}$, b, C_{11}, C_{12}, and ε , are dependent on In composition (χ_i).

$$\varepsilon = \frac{a_{sub}-a_{epi}}{a_{epi}} = \frac{a_{GaAs}-a_{InGaAs}}{a_{InGaAs}} \tag{20}$$

$\varepsilon < 0$ represents a compressive strain while $\varepsilon > 0$ represents a tensile strain.

The direction of band shift depends on the sign of ε, and Figure 2.4 shows schematically the energy dispersion in the parabolic band approximation for different ε values.

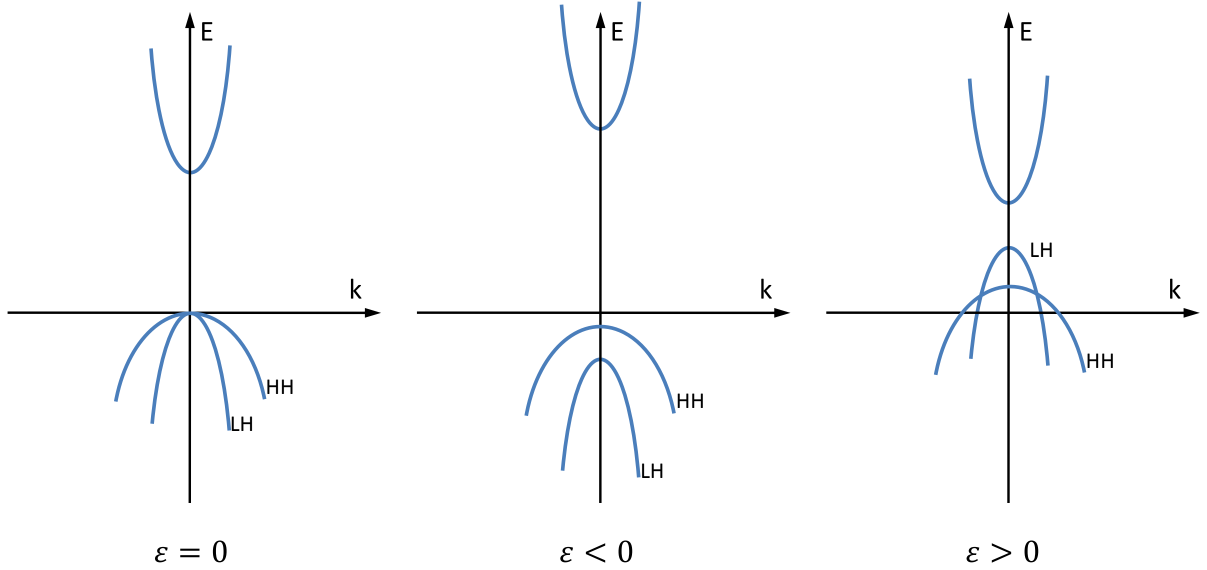

Fig. 2.4 Schematic of energy dispersion in the parabolic band approximation for different ε values

$GaAs$ and $In_{\chi_i}Ga_{(1-\chi_i)}As$ are known as direct band gap ($\Gamma-\Gamma$ valley transition) semiconductors, and In composition (χ_i) plays an important role in modifying the band gap of $In_{\chi_i}Ga_{(1-\chi_i)}As$ ternary alloy. $In_{\chi_i}Ga_{(1-\chi_i)}As$ ternary alloy can be regarded as a mixture of $GaAs$ and $InAs$ binary compounds. The dependence of energy band gap on In composition (χ_i) is assumed to fit a simple quadratic form.

$$Eg_{In_{\chi_i}Ga_{(1-\chi_i)}As(unstrained)} = \chi_i E_{InAs} + (1-\chi_i)E_{GaAs} - \chi_i(1-\chi_i)C_\Gamma \quad (21)$$

where the so-called bowing parameter C_Γ accounts for the deviation from a linear interpolation between $GaAs$ and $InAs$. The conventional value of C_Γ for $In_{\chi_i}Ga_{(1-\chi_i)}As$ is in the range of 0.47 to 0.49 eV.

Chapter 3

Results and Discussion

3.1 Capping Layer-Induced Energy Shift via Thermal Treatment

The samples used in this study were all grown on $(0\ 0\ 1)$ semi-insulating $GaAs$ substrates by a Veeco Gen II molecular beam (MBE) epitaxy system. Both SiO_2 and TiO_2 dielectric capping films, were deposited by an E-gun evaporator. In order to initiate the interdiffusion process, post-growth rapid thermal annealing (RTA) was utilized to provide high temperature circumstances up to 925 ℃.

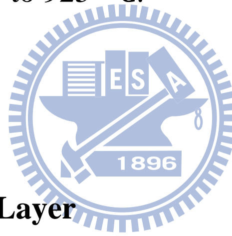

3.1.1 Influence of SiO_2 Capping Layer

The schematic structure of sample A used to evaluate the influence of SiO_2 capping layer on the $InGaAs/GaAs$ quantum well intermixing is shown in Fig. 3.1. The $(0\ 0\ 1)$ semi-insulating GaAs substrate was first grown with a superlattice with 10 pairs of 5 nm $GaAs$ wells and 5 nm $AlAs$ barriers and a 100 nm $GaAs$ buffer layer, and then it was ready to grow the designed structure. The single quantum well structure was grown as a 6 nm $In_{0.22}Ga_{0.78}As$ well sandwiched by two 6 nm $GaAs$ barriers. The 30 nm and 1 μm $Al_{0.4}GaAs$ layers were grown on the top and bottom of the $InGaAs/GaAs$ quantum well respectively so as to provide a better confinement of electrons inside the quantum well. The top 10 nm $GaAs$ layer protected the underlying layers from oxidized. The SiO_2 capping films were deposited to the thickness of 150 nm by an E-gun evaporator.

Layer	Thickness	
SiO_2	150 nm	
GaAs	10 nm	
$Al_{0.4}GaAs$	30 nm	
GaAs	6 nm	
$In_{0.22}GaAs$	6 nm	
GaAs	6 nm	
$Al_{0.4}GaAs$	1 μm	
Buffer GaAs	100 nm	
GaAs	5 nm	Superlattice of 10-pair GaAs / AlAs
AlAs	5 nm	
GaAs S. I. Substrate		

Fig. 3.1 The schematic epitaxy structure of sample A which was designed for a $In_{0.22}Ga_{0.78}As/GaAs$ single quantum well. The capping layer of 150 nm SiO_2 film was deposited on the top of the semiconductor surface.

The photoluminescence spectra in this section were measured at 77 K with 488 nm argon laser as the optical pumping source. The emission wavelength of the as-grown sample is at 939 nm, and its full width at half maximum (FWHM) is about 15.2 meV. Fig. 3.2 shows the 77 K photoluminescence spectra of the samples processed at various RTA temperatures from 800 ℃ to 925 ℃. The corresponding peak position of each sample is extracted from Fig. 3.2 and listed in Table 3.1.

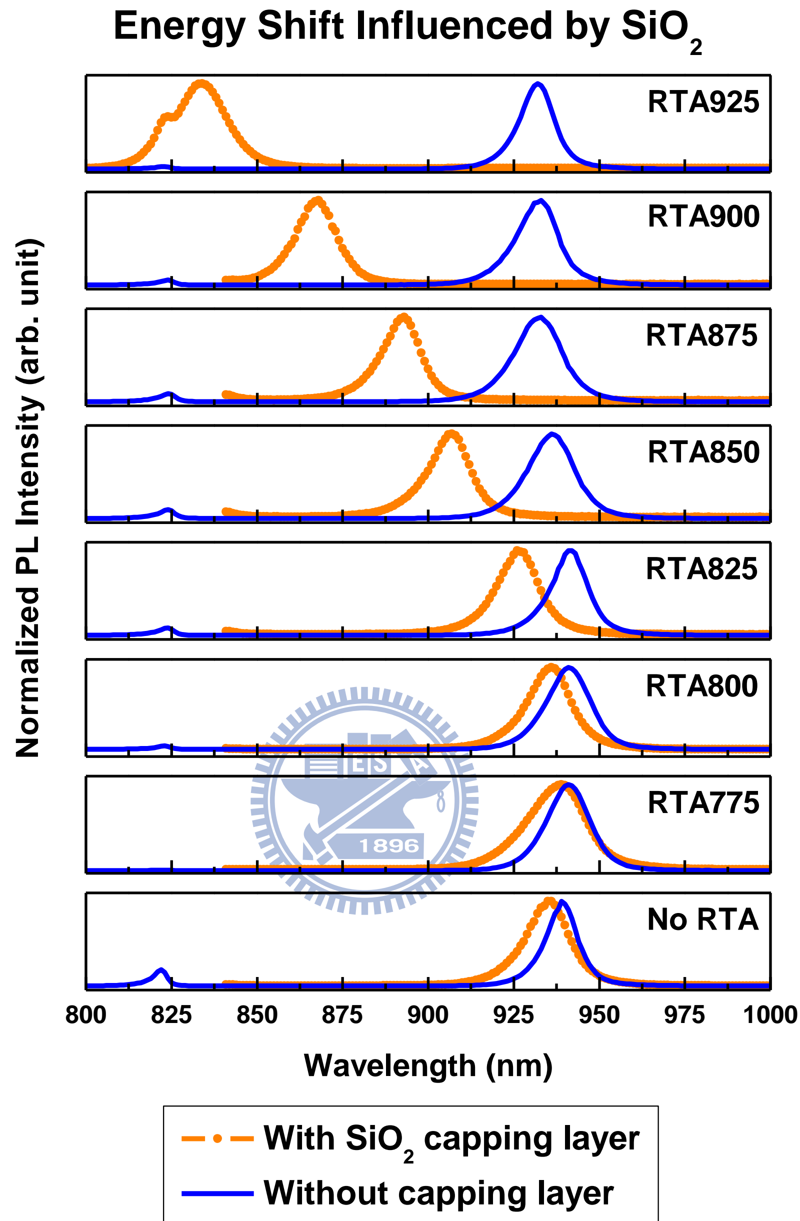

Fig. 3.2 The photoluminescence spectra measured at 77 K. The samples were treated with rapid thermal annealing (RTA) at various temperatures (No RTA, RTA at 775, 800, 825, 850, 875, 900, 925 ℃). The solid lines represent the samples without capping layers while the dashed lines represent the samples with 150 nm SiO_2 capping layers.

Table 3.1 The detailed data extracted from Fig. 3.2 of sample A

	Data obtained from photoluminscence spectra at 77 K				
	Without capping layer		**With SiO_2 capping layer**		
RTA	**Peak Position (nm)**	**Energy (eV)**	**Peak Position (nm)**	**Energy (eV)**	**Energy shift (meV)**
No	939	1.321	935	1.326	5.65
775	941	1.318	939	1.321	2.81
800	941	1.318	936	1.325	7.04
825	941	1.318	926	1.339	21.35
850	936	1.325	907	1.367	42.36
875	933	1.329	893	1.389	59.53
900	933	1.329	868	1.429	99.53
925	932	1.330	834	1.487	156.34

where energy shift at certain RTA temperature T_i is defined as $\Delta E(T_i)$ in Eq. (22).

$$\Delta E(T_i) = E_{with\ SiO_2\ capping\ layer}(T_i) - E_{without\ capping\ layer}(T_i) \qquad (22)$$

The higher the RTA temperature was used, the more evident separation we found between the samples with capping layers and those without capping layers. The emission lengths of the samples without capping layers stayed almost the same with only slight variation. On the contrary, the samples with SiO_2 capping layers show drastic blue-shifts with increasing RTA temperature. That is to say, SiO_2 indeed enhance the quantum well intermixing, especially at higher RTA temperature. After annealing at 900 ℃ for 30 seconds, the emission peak shows a blue-shift of about 100 meV. The sample capped with SiO_2 and annealed at 925 ℃ indeed shows an even larger blue-shift. Yet, the peak we concerned merges with the $GaAs$ peak around 824 nm, and this unwanted overlapping may make analysis more complicated.

In order to achieve complete disordering, the annealing time used in other approaches should be as long as several hours [22]. However, less than 1 minute is enough in the case of SiO_2-enhanced quantum well intermixing. Although the annealing time we used was as short as 30 seconds, the obvious energy shift of the samples with SiO_2 capping layers still can be

observed. It implies that the SiO_2-assisted interdiffusion rate of In and Ga atoms is substantially higher.

As for the full width at half maximum (FWHM) of the emission peak, the variation tendency with increasing RTA temperature seems to be irregular. The emission peak becomes broader when relatively lower-temperature annealing is applied, and it once again turns into a narrow peak when the annealing is processed at high temperature above 900 ℃. The broadening may come from the non-uniform distribution of the degree of intermixing throughout the sample. Annealing below 900 ℃ can induce the interdiffusion of In and Ga atoms, but the energy provided is not large enough for all atoms move simultaneously. Higher RTA temperature not only leads to a larger blue-shift but also contributes to the uniformity in the quantum well intermixing.

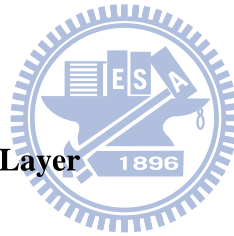

3.1.2 Influence of TiO$_2$ Capping Layer

The schematic structure of sample B used to evaluate the influence of TiO_2 capping layer on the $InGaAs/GaAs$ quantum well intermixing is shown in Fig. 3.3. The single quantum well structure was grown as a 3 nm $In_{0.27}Ga_{0.73}As$ well sandwiched by two 6 nm $GaAs$ barriers. Except for the quantum well design, the structure of other layers was the same as the structure in sample A. The TiO_2 capping films were deposited to the thickness of 200 nm by an E-gun evaporator.

TiO_2 films influence the quantum well intermixing in a similar manner to the SiO_2 capping layer but in a completely opposite way. From Table 2.1, the thermal expansion coefficient of TiO_2 is larger than $InGaAs$ and $GaAs$. Therefore, few Ga vacancies (V_{Ga}) are generated at the TiO_2-$GaAs$ interface, and the tensile strain in the top $GaAs$ layer tends to trap Ga vacancies and impede the interdiffusion of In and Ga atoms.

TiO_2	200 nm
GaAs	10 nm
$Al_{0.4}GaAs$	30 nm
GaAs	6 nm
$In_{0.27}GaAs$	3 nm
GaAs	6 nm
$Al_{0.4}GaAs$	1 μm
GaAs	5 nm
AlAs	5 nm
Buffer GaAs	100 nm
GaAs S. I. Substrate	

Superlattice of 10-pair GaAs / AlAs

Fig. 3.3 The schematic epitaxy structure of sample B which was designed for a $In_{0.27}Ga_{0.73}As/GaAs$ single quantum well. The capping layer of 200 nm TiO_2 film was deposited on the top of the semiconductor surface.

The photoluminescence spectra in this section were measured at 25 K with 488 nm argon laser as the optical pumping source. The emission wavelength of the as-grown sample is at 914 nm, and its full width at half maximum (FWHM) is about 26.5 meV. Fig. 3.4 shows the 25 K photoluminescence spectra of the samples processed at various RTA temperatures from 850 ℃ to 900 ℃. The corresponding peak position of each sample is extracted from Fig. 3.4 and listed in Table 3.2.

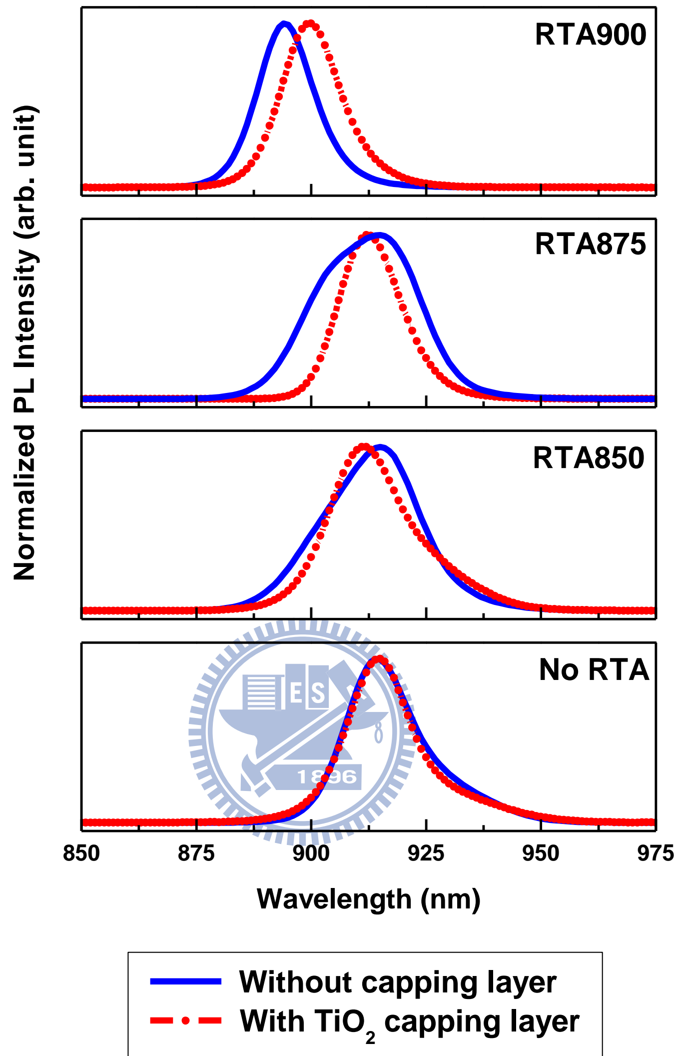

Fig. 3.4 The photoluminescence spectra measured at 25 K. The samples were treated with rapid thermal annealing (RTA) at various temperatures (No RTA, RTA at 850, 875, 900 °C). The solid lines represent the samples without capping layers while the dashed lines represent the samples with 200 nm TiO_2 capping layers.

The TiO_2 capping layer functions as an inhibitor of the interdiffusion of In and Ga atoms because its relatively large thermal expansion coefficient creates tensile stress for the underlying $GaAs$ layer. The tensile strain field limits the degree of quantum well intermixing, and an obvious energy red-shift can be found in photoluminescence spectra.

Table 3.2 The detailed data extracted from Fig. 3.4 of sample B

	Data obtained from photoluminscence spectra at 25 K				
	Without capping layer		**With TiO_2 capping layer**		
RTA	**Peak Position (nm)**	**Energy (eV)**	**Peak Position (nm)**	**Energy (eV)**	**Energy shift (meV)**
No	914	1.357	914	1.357	0.00
850	914	1.357	911	1.361	4.47
875	914	1.357	912	1.360	2.98
900	894	1.387	900	1.378	-9.25

where energy shift at certain RTA temperature T_i is defined as $\Delta E(T_i)$ in Eq. (23).

$$\Delta E(T_i) = E_{with\ TiO_2\ capping\ layer}(T_i) - E_{without\ capping\ layer}(T_i) \tag{23}$$

The emission peaks of the samples both with and without TiO_2 capping layers kept at the same position of the as-grown sample when the RTA temperature was set below 900 °C. The energy shift smaller than 5 meV can be seen as a negligible experimental error. When the RTA temperature was raised to 900 °C, the sample without capping layer had an energy red-shift of 30 meV while the sample with TiO_2 capping layer had a comparatively small energy red-shift of 21 meV. A meaningful energy red-shift of about 10 meV can be regarded as an evident of TiO_2-impeded quantum well intermixing.

The apparent large full width at half maximum (FWHM) of the uncapped sample annealed at a middle RTA temperature of 875 °C can be explained as the serious non-uniformity in the degree of quantum well intermixing. By comparison, no obvious broadening is found for the samples capped with TiO_2 layers. The samples with TiO_2 capping layers show such a slight degree of quantum well intermixing that the variation of

uniformity throughout the sample barely influence the FWHM of the emission peak.

In order to clearly illustrate the effects of SiO_2 and TiO_2 on the quantum well intermixing, the relation between the energy shift and the corresponding RTA temperature is plotted in Fig. 3.5. SiO_2-enhanced quantum well intermixing can be inferred from the nearly exponential increase of energy shift with increasing RTA temperature. The small but meaningful energy red-shift of the sample capped with TiO_2 layer and annealed at 875 ℃ implies the ability of TiO_2 to inhibit quantum well intermixing.

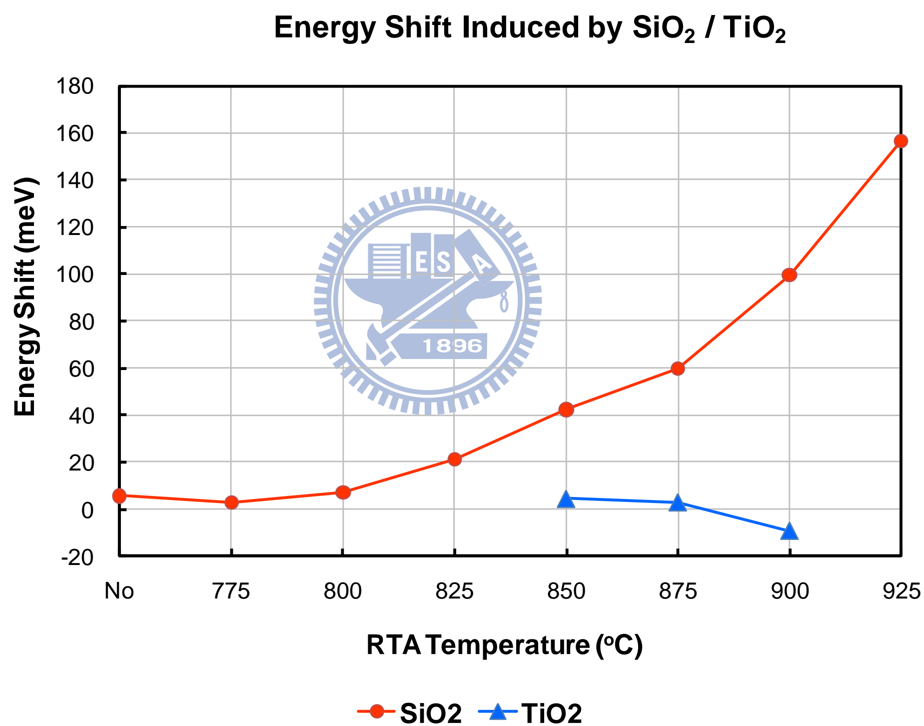

Fig. 3.5 Energy shifts at various temperature induced by SiO_2 and TiO_2 capping layers. The red dots represent sample A with SiO_2 capping layer, and the blue triangles represent sample B with TiO_2 capping layer. The value of energy shift is positive for a blue-shift and negative for a red-shift.

3.2 Selective Quantum Well Intermixing via Patterned SiO_2 Layer

For the purpose of selective area wavelength tuning of $InGaAs/GaAs$ quantum well, SiO_2 capping layer was patterned to be a mask. The patterning techniques used in this study were either lift-off lithography or electron-beam (e-beam) lithography. The method of e-beam lithography combined with subsequent reactive ion etching (RIE) was utilized for the fabrication of nanometer-scale patterns. Rapid thermal annealing at 875 ℃ was performed after lithography process so as to activate the quantum well intermixing mechanism. Finally, micro-photoluminescence spectroscopy (micro-PL) was used to examine the optical properties of the samples.

3.2.1 Spatial Resolution of Micro-Photoluminescence

1896

The epitaxy structure of sample C was the same as sample B which consisted mainly of $In_{0.27}Ga_{0.73}As/GaAs$ single quantum well. Fig. 3.6 illustrates the process flow of the fabrication of sample C with mesa patterns which are around 10 μm in diameter. TiO_2 films were deposited after photoresist (PR) coating on the surface of the semiconductor, and then lift-off lithography technique was utilized to make the mesa patterns. Afterwards, the entire sample surface was coated with SiO_2 films. TiO_2 and SiO_2 films used here were deposited by an E-gun evaporator and the thickness were 200 nm and 150 nm respectively.

According to the results discussed in section 3.1, the mesa patterns capped with TiO_2 layer performed locally impeded-quantum well intermixing. Since the SiO_2 layer on top of the TiO_2 layer had no direct contact with the underlying semiconductor, it exerted no effect on the quantum well in the regions below the mesa structures.

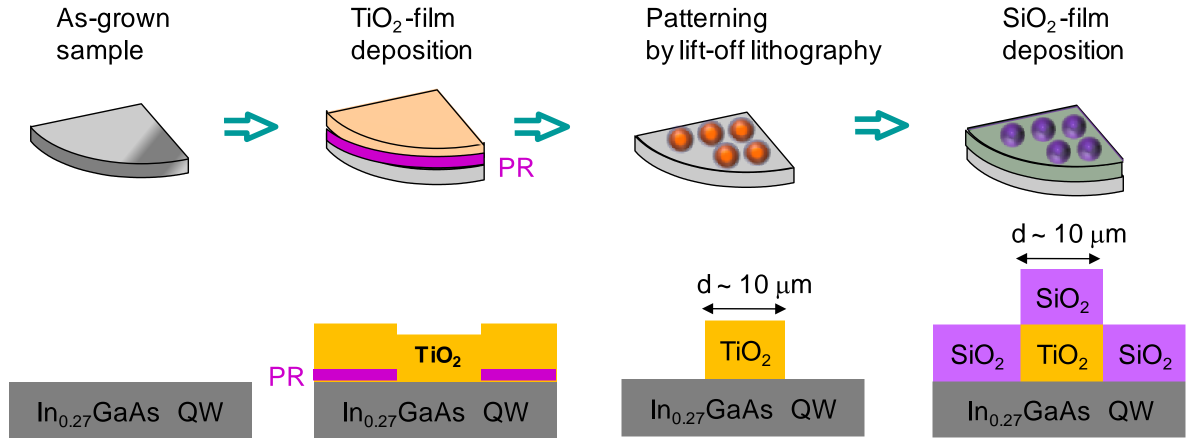

Fig. 3.6 Process flow of sample C fabrication.

From the scanning electron microscopy graphs in Fig. 3.7, the size of the hexagonal mesa patterns is about 9.5 μm, and the mesa structures can be easily observed. Both photoluminescence (PL) and micro-photoluminescence (micro-PL) spectra were measured for sample C. Laser beam size was the major difference between PL and micro-PL, that is to say, the area of sample surface covered in each measurement differed. The laser beam size of PL was close to 100 μm while the laser beam size of micro-PL was only 10 μm which was approximately equal to the size of mesa patterns.

When measuring PL spectra, the laser-coverage area contained both TiO_2 and SiO_2-dominated regions. Fig. 3.7 (b) schematically shows the covered area by the PL laser beam. On the other hand, the size of micro-PL laser beam was small enough that the regions inside and outside the mesa patterns can be measured separately. In Fig. 3.7 (C), position (1) and (2) indicate two individual spectra which were measured by focusing the micro-PL laser beam on the TiO_2-governed (inside the mesa) or SiO_2-governed regions (outside the mesa).

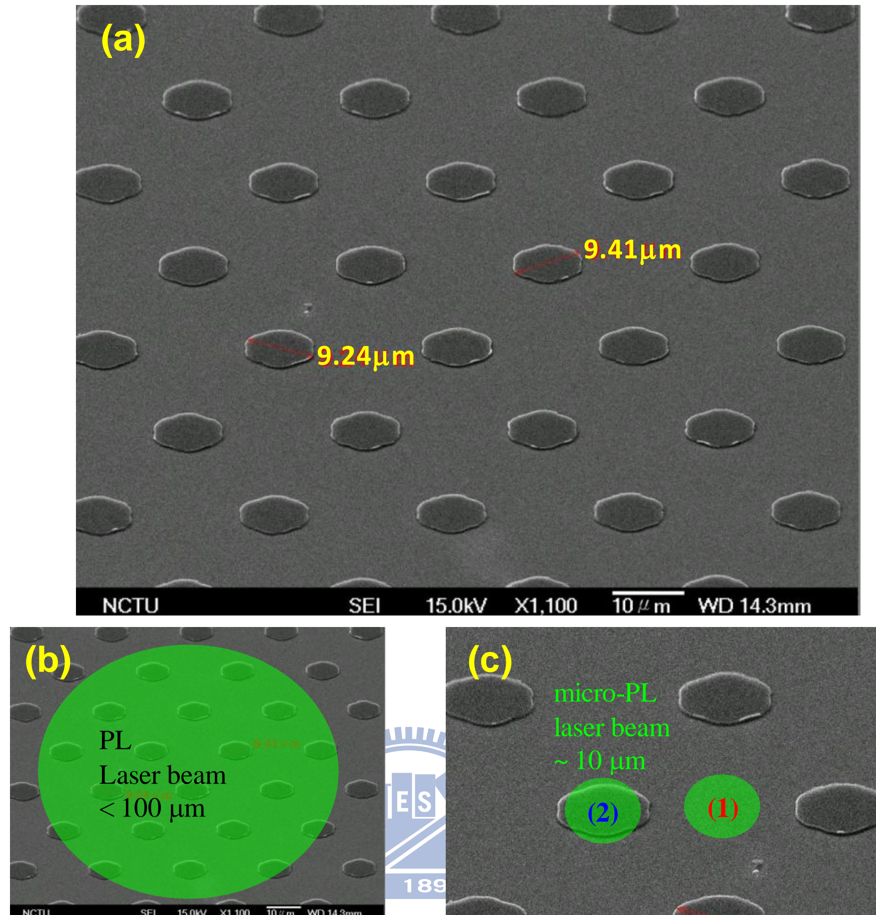

Fig. 3.7 SEM micrographs of sample C. (a) The size of the hexagonal mesa is about 9.5 μm. (b) Schematic illustration of the coverage area by the PL laser beam. (c) Schematic illustration of the coverage area by the micro-PL laser beam. Position (1) and (2) indicates that the micro-PL laser beam is focused inside and outside the mesa respectively.

The photoluminescence (PL) and micro-photoluminescence (micro-PL) spectra measured at 77 K are shown in Fig. 3.8. The black line with diamond-like symbols is the PL spectrum. An emission peak with comparatively higher intensity and shorter wavelength overlaps with another emission peak with comparatively lower intensity and longer

wavelength. The red dot dashed represents the micro-PL spectrum measured at position (1) where the $GaAs$ layer directly contacted with SiO layer, and the corresponding emission peak is located at 898 nm. Likewise, the blue dashed line represents the micro-PL spectrum measured at position (2) where the $GaAs$ layer directly contacted with TiO layer, and the corresponding emission wavelength is 916 nm.

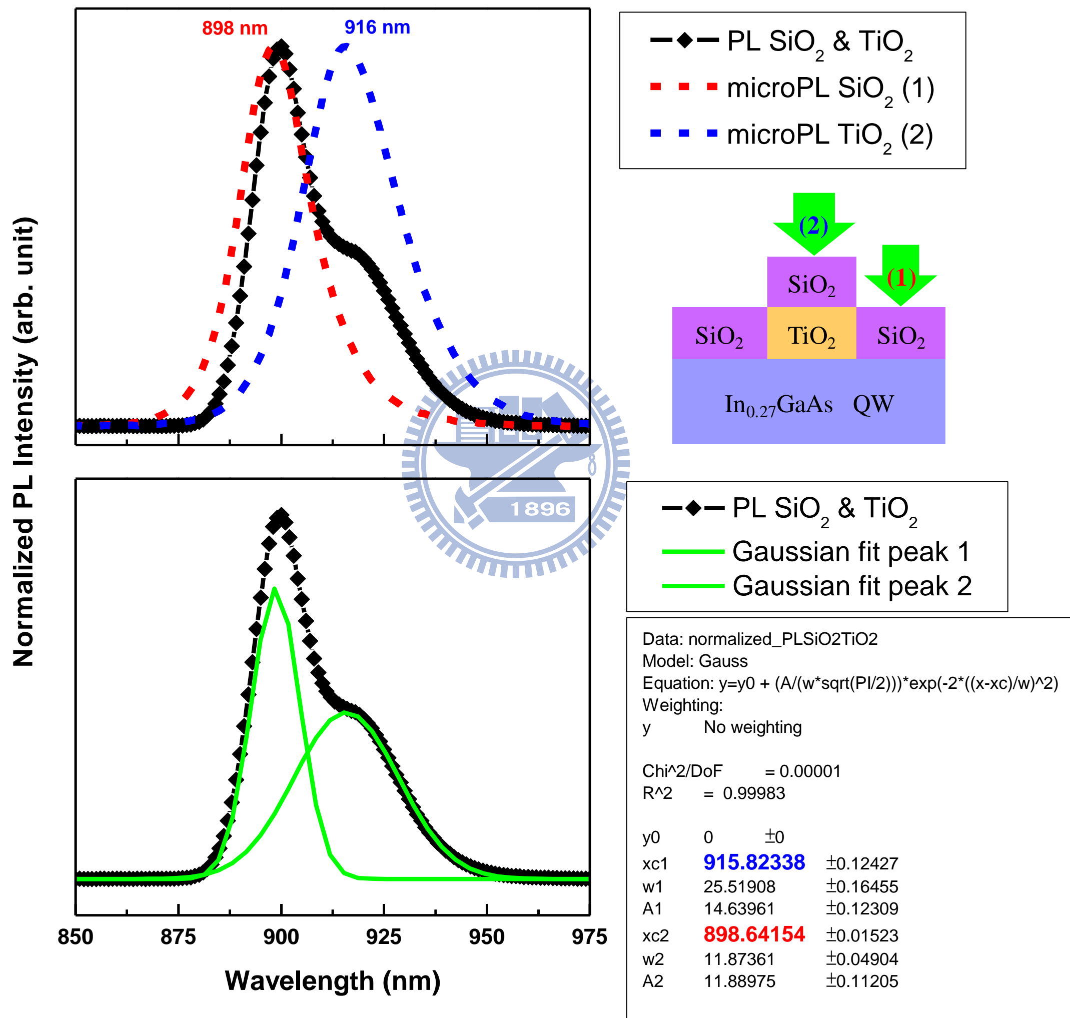

Fig. 3.8 The photoluminescence and micro-photoluminescence spectra measured at 77 K. The upper figure combines one PL spectrum and two micro-PL spectra measured at position (1) and (2). The lower figure shows the results of peak analysis by Gaussian fitting.

The PL spectrum implies a combination of two individual peaks. Thus, we utilized the method of Gaussian fitting to analyze this multi-peak, and the detailed information is shown in the lower part of Fig. 3.8. Two individual peaks located at 898.6 nm and 915.8 nm were extracted from the PL spectrum, and these two wavelengths perfectly agree with those two emission peaks in the micro-PL spectra.

All in all, micro-PL provides better spatial resolution than PL because the laser beam shrinks in size when passing through objective lens. If the emission wavelengths from the regions inside and outside the patterns are too close to be distinguished, micro-PL is the better alternative to investigate selective area interdiffusion.

3.2.2 Aperture Size-Dependent Energy Shift

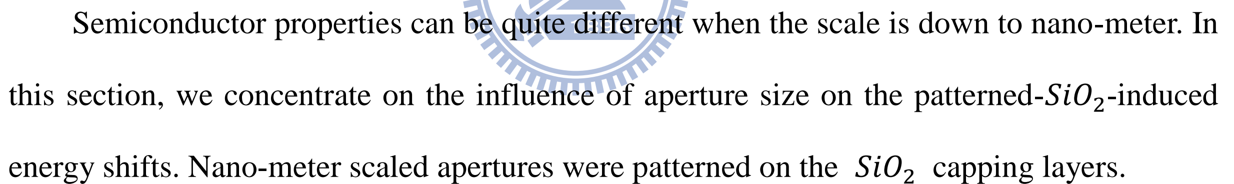

Semiconductor properties can be quite different when the scale is down to nano-meter. In this section, we concentrate on the influence of aperture size on the patterned-SiO_2-induced energy shifts. Nano-meter scaled apertures were patterned on the SiO_2 capping layers.

As mentioned in section 3.1, the energy shift caused by TiO_2 capping layer at RTA temperature of 875 ℃ can barely be distinguished, although TiO_2 indeed made contribution to inhibiting FWHM from broadening. For the sake of practicability and convenience during the fabrication of nanometer-scaled patterns, we skipped the procedure of TiO_2 deposition and replaced lift-off lithography with e-beam lithography and reactive ion etching (RIE). The structure of the sample used here is the same as sample A, including the epitaxy structure and the growing condition of SiO_2 capping layers. The fabrication process flow is illustrated in Fig. 3.9.

The SiO_2 capping layer was patterned with circular apertures in various diameters (d = 55, 75, 100, 125, 135 nm). The apertures with the same diameter were arranged in an array, of which the periodicity is 200 nm.

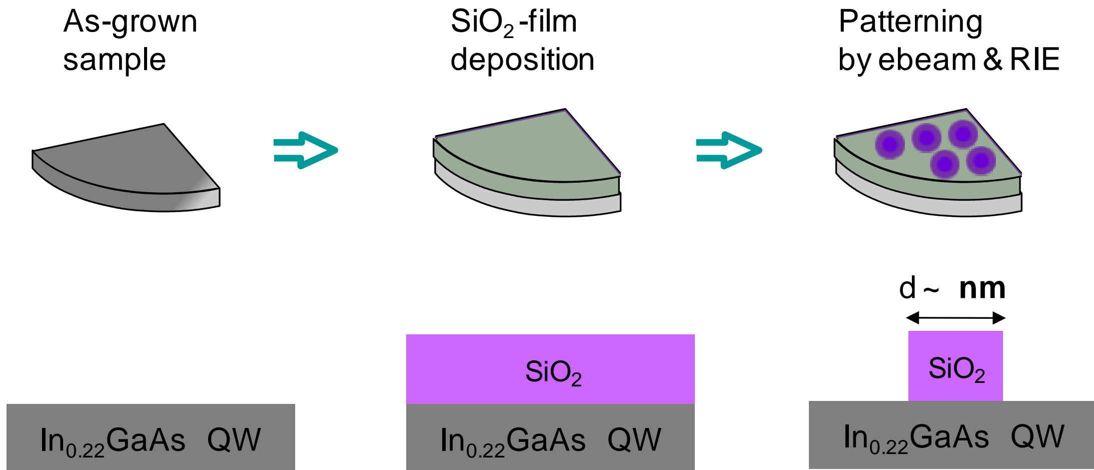

1896

Fig. 3.9 Process flow of patterning SiO_2 capping layer by e-beam and RIE.

Scanning electron microscopy (SEM) was used to examine the diameter of apertures. The SEM pictures in Fig. 3.10 display two arrays, of which the diameter of apertures is 75 nm and 100 nm repectively.

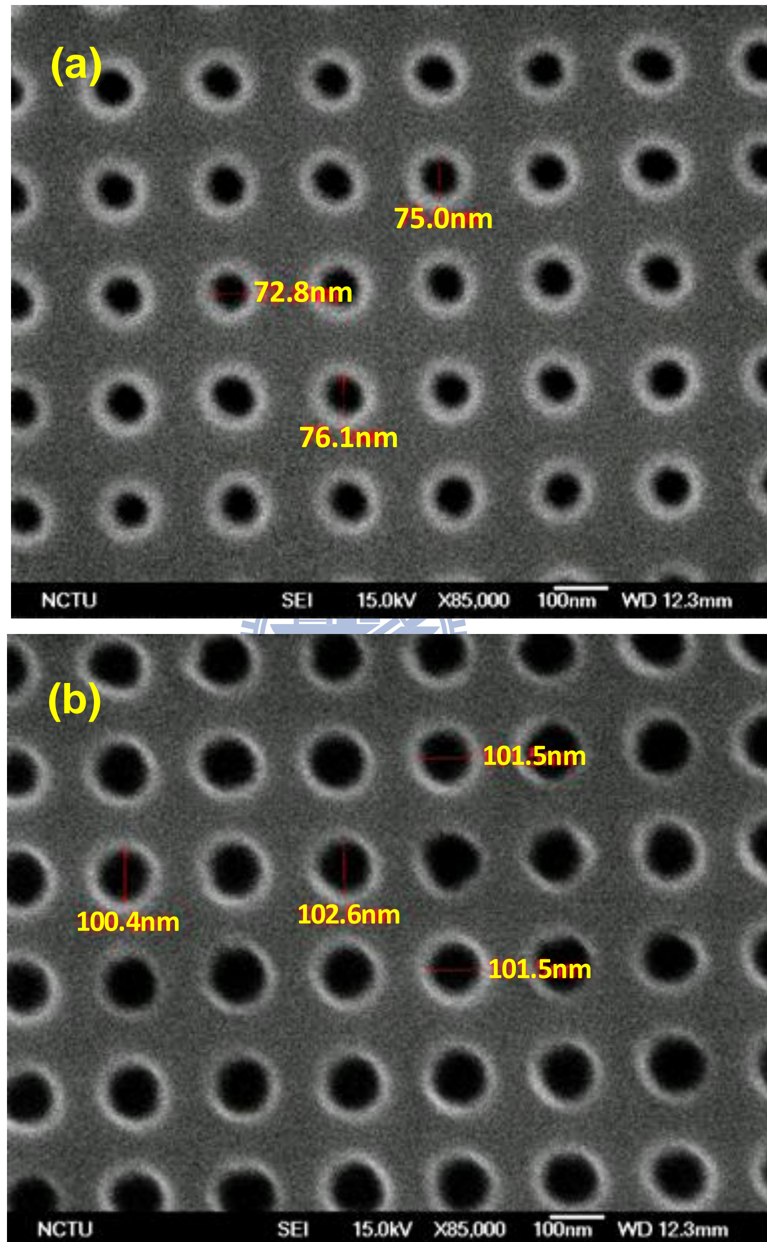

Fig. 3.10 SEM micrographs of the patterns on the SiO_2 capping layers. (a) and (b) shows the circular apertures are 75 nm and 100 nm in diameter respectively. The periodicity of both (a) and (b) is 200 nm.

The patterned samples were annealed at RTA 875 ℃ and 900 ℃ and measured by micro-photoluminescence (micro-PL) at 77 K shown in Fig. 3.11. Since the size of designed patterns (d is in the range of 55 nm to 135 nm) was much smaller than the micro-PL laser beam size (10μm), inevitably the area both inside and outside apertures were covered by the laser beam. Theoretically, two emission peaks should exist concurrently in a micro-PL spectrum. The higher-energy peak stands for the area outside apertures while the lower-energy peak stands for the area inside apertures. However, general semiconductor properties suggest that electrons prefer staying at lower-energy states and the diffusion length of electrons in $GaAs$ can be larger than 5 μm. As a result, electrons not only move toward but also accumulate in the regions inside apertures, and then only few electrons remaining outside apertures can contribute to the emission in the higher-energy state. The emission peak we concerned is the lower-energy one which emitted from the regions inside apertures, where the SiO_2 capping layer is removed completely and SiO_2-induced quantum well intermixing should not happen.

In an idea case or the case considering micrometer-scaled apertures, no obvious energy shift would be found in the regions inside apertures. It implies that Ga vacancies in the adjacent regions under SiO_2 capping layer hardly diffuse across the boundary. That would totally not be the case when the size of apertures is scaled down to nanometer.

Ga vacancies (V_{Ga}) diffuse downward to $InGaAs/GaAs$ quantum well and induce the interdiffusion of Ga and In atoms. In the meantime, Ga vacancies (V_{Ga}) diffuse laterally toward the adjacent regions without SiO_2 capping layer as well. As a consequence, the regions inside apertures is also affected by quantum well intermixing. When the size of apertures is getting small, the lateral diffusion effect becomes more influential. Presumably, the effective diameter of apertures is limited to a specific minimum value for each RTA temperature. That is to say, if the diameter of apertures is smaller than the effective minimum, all of the regions inside apertures will suffer quantum well intermixing thoroughly and

aperture-influenced selective area quantum well intermixing will no longer be valid.

In the case of RTA 875 ℃, the emission peak from the regions capped with non-patterned SiO_2 layer was located at 893 nm equivalent to 1.389 eV, and the emission peak from the sample uncapped with SiO_2 layer is located at 933 nm equivalent to 1.329 eV. The aperture-dependent energy shifts can be easily found from the micro-photoluminescence spectra shown in Fig. 3.11. When the diameter is getting smaller, the emission peak from the regions inside apertures becomes closer to the peak from the regions capped with non-patterned SiO_2 layer.

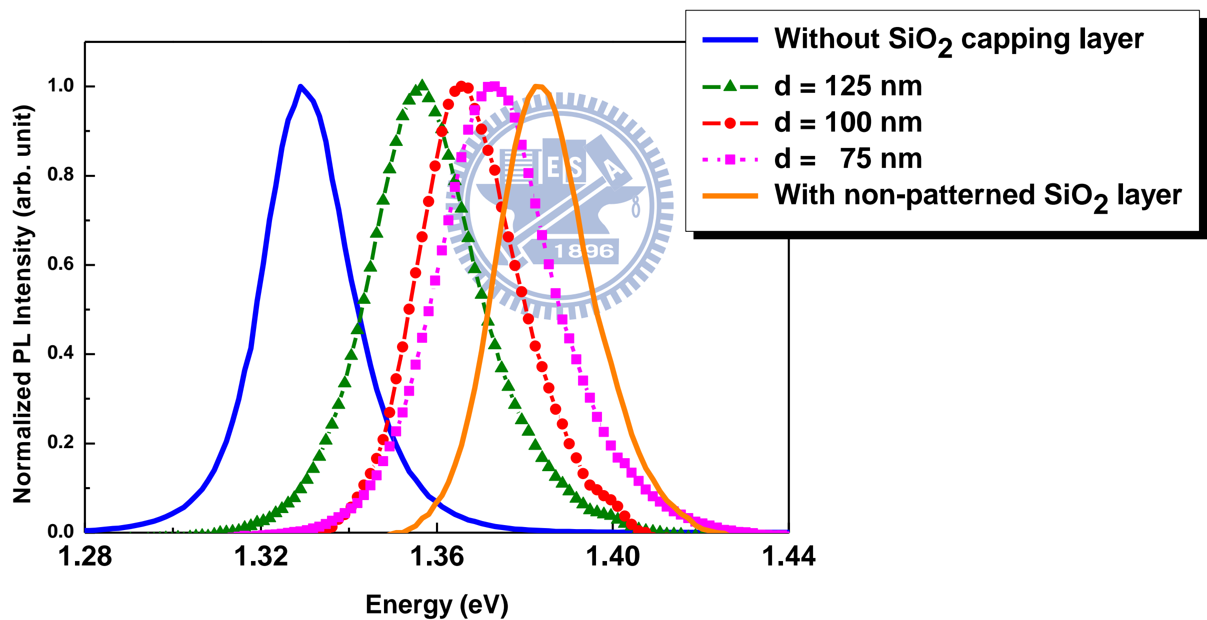

Fig. 3.11 The micro-photoluminescence spectra measured at 77 K. The orange solid curve represents the sample capped with non-patterned SiO_2 capping layer. The blue solid line represents the sample without SiO_2 capping layer. The lines with symbols (pink squares, red circles, and green triangles) represent the patterned samples (d = 75, 100, 125 nm).

The energy shift of the sample with apertures in a specific diameter is equal to its emission energy minus the emission energy of the sample without SiO_2 capping layer annealed at the same RTA temperature, shown in Eq. (24).

$$\Delta E(d,T) = E(d,T) - E_{uncapped\ with\ SiO_2}(T) \tag{24}$$

In Fig. 3.12, the red short-dashed line indicates the highest energy-shift level of the samples with SiO_2 capping layer annealed at 875 °C. Similarly, the green dot-dashed line indicates the highest energy-shift level of the samples with SiO_2 capping layer annealed at 900 °C.

In the case of RTA 900 °C, the emission peak from the regions capped with non-patterned SiO_2 layer was located at 862 nm equivalent to 1.439 eV, and the emission peak from the sample uncapped with SiO_2 layer is located at 933 nm equivalent to 1.329 eV.

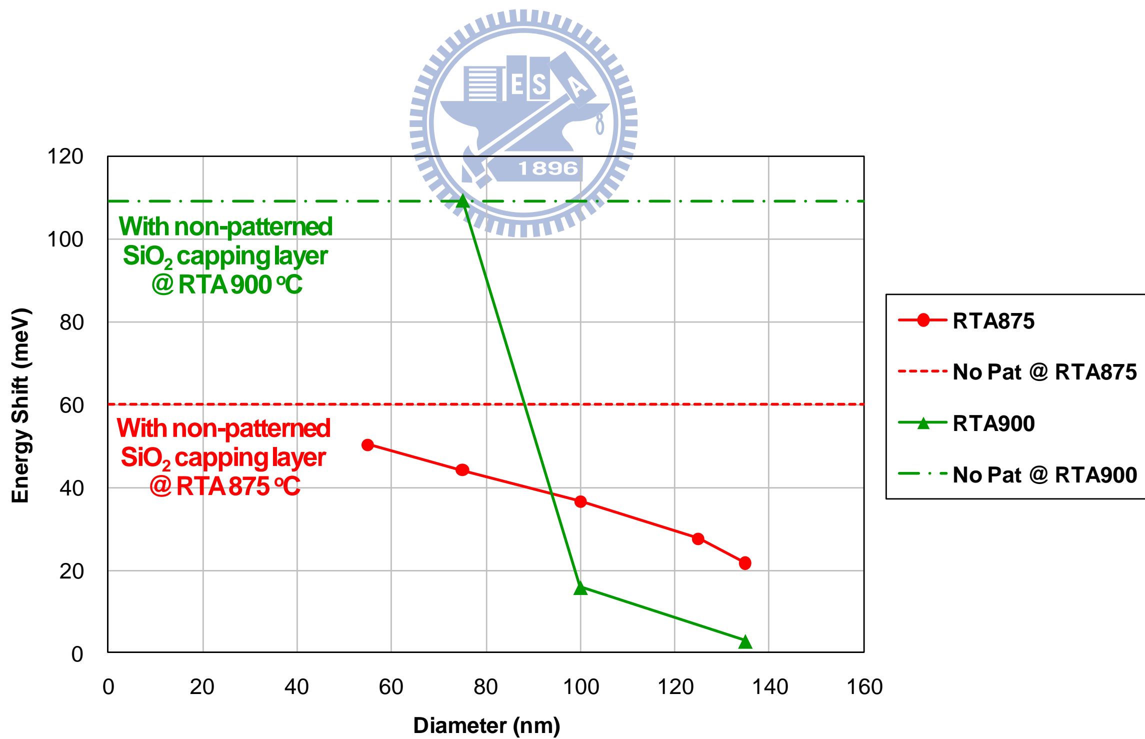

Fig. 3.12 Diameter-dependent energy shifts of the patterned samples annealed at 875 and 900 °C. The lines and circular symbols in red color represent the samples annealed at 875°C. The lines and triangular symbols in green color represent the samples annealed at 900°C.

According to section 3.1.1, we know that the degree of quantum well intermixing becomes greater as the RTA temperature increases. In Fig. 3.12, the samples annealed at 900 ℃ show an even more severe effect of aperture-dependent energy shift. It implies that the case of RTA 900 ℃, in which the minimum effective diameter is 75 nm, cannot achieve the goal of three-dimensional (3D) quantum dot (QD) confinement. The self-assembled $InAs$ QDs grown by a Veeco Gen II molecular beam (MBE) epitaxy system in our laboratory are 40nm to 60 nm in diameter. For this reason, we expect that the fabrication of artificial quantum dot confinement is possible to accomplish when the minimum effective diameter can be controlled under 50 nm. From the curve of RTA 875 ℃ in Fig. 3.12, we infer that it may be feasible to design apertures with diameter smaller than 50 nm under the condition of applying rapid thermal annealing at 875 ℃.

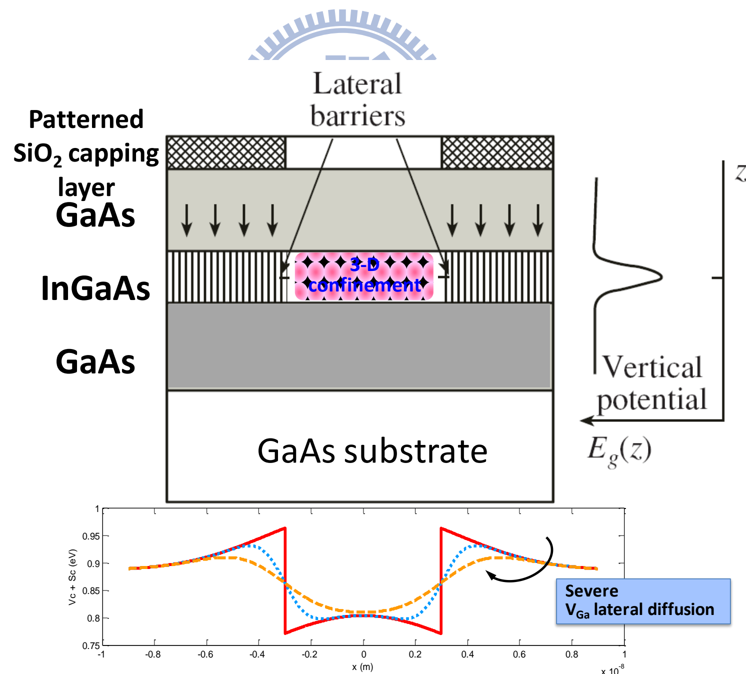

Fig. 3.13 Schematic of three-dimensional (3D) confinement by selective area $InGaAs$ / $GaAs$ quantum well intermixing. The lateral potential profiles were simulated for different degree of V_{Ga} lateral diffusion.

The basic idea of artificial quantum dot confinement fabricated by the method of selective area quantum well intermixing is illustrated in Fig. 3.13. In-plane (xy plane) lateral potential can be established by the use of patterned SiO_2 capping layer while the interdiffusion along the growth-direction (z-direction) leads to vertical potential. A three-dimensional (3D) confined potential is then created under the regions inside apertures.

The production of quantum dots by selective interdiffusion has already been reported in $CdTe/CdMgTe$ quantum well system[23]. This successful case reinforces our confidence in the possibility of artificial quantum dot manufactured in $InGaAs/GaAs$ quantum well system.

3.2.3 Excitation Power-Dependent Emission Peak

Photoluminescence spectra strongly depend on the excitation power, and the spectra obtained by applying various excitation powers can be drastically different even if the identical sample is measured. Excitation power density is directly associated with pumped-electron density in the measurement.

The structure of the sample used in this section is the same as sample A, including the epitaxy structure ($In_{0.22}Ga_{0.78}As/GaAs$ single quantum well) and the growing condition of SiO_2 capping layers. The SiO_2 capping layer was patterned as an array of circular apertures. The diameter and the periodicity of the circular apertures are 50 nm and 500 nm respectively (d = 75 nm; P = 500 nm). Fig. 3.14 shows the schematic illustration of the patterned SiO_2 capping layer. Rapid thermal annealing at 875 ℃ for 30 seconds is performed before the micro-photoluminescence (micro-PL) measurement at 77 K.

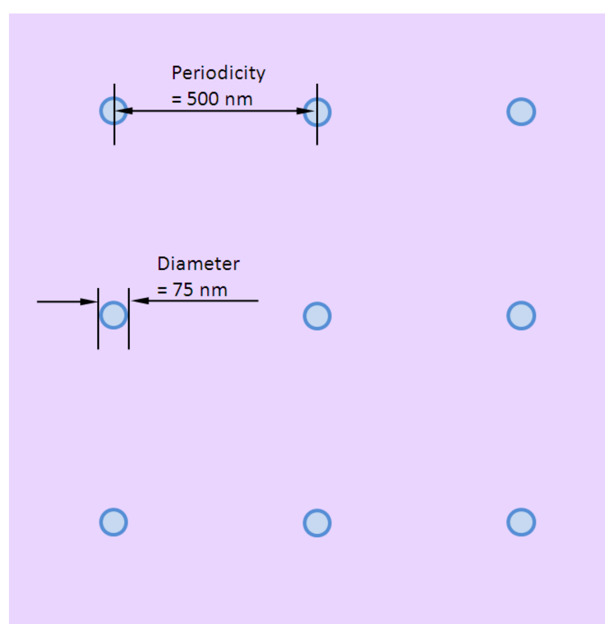

Fig. 3.14 Schematic of the pattern designed as an array of circular apertures. The diameter of the circular apertures is 75 nm, and the periodicity is 500 nm. (d = 75 nm; P = 500 nm)

Fig. 3.15 shows the micro-photoluminescence (micro-PL) spectra measured at 77 K, and each curve represents one excitation power. In order to investigate the transformation of PL spectrum with increasing excitation power, the magnitude of PL intensity in each spectrum was not normalized. Furthermore, all of the experimental conditions and parameters, only except for excitation power, were kept identical, and thus the comparison is convincing.

Higher excitation power undoubtedly pumps more electrons to the sample, and more electrons contribute to larger PL intensity. Nonetheless, the magnification of the emission peak at about 1.33 eV does not follow a uniform scale-up tendency. As excitation power increases, the peak shape gets further away from Gaussian distribution. The emission peak expands more enormously toward the higher-energy side and shows a shoulder-like side peak. If applying even higher excitation power, another peak appears at around 1.45 eV.

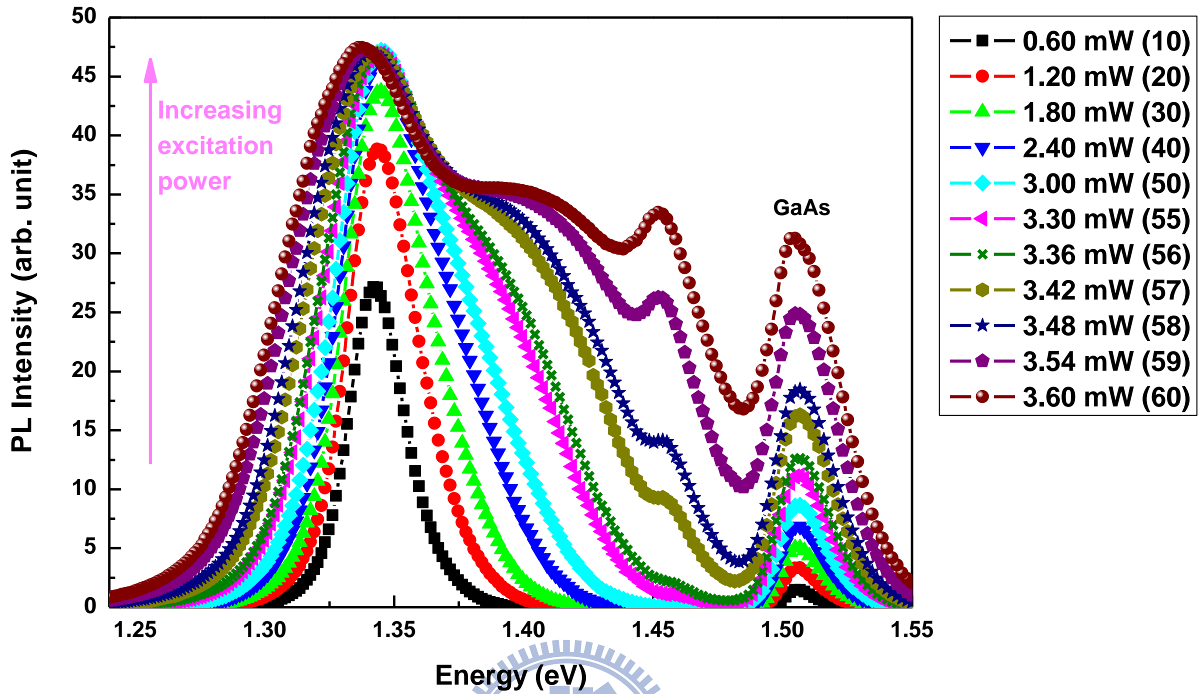

Fig. 3.15 The power-dependent micro-photoluminescence spectra of the sample with patterned SiO_2 capping layer (d = 75 nm; P = 500 nm).

It is well-known that electrons tend to fill in the unoccupied lowest-energy states. Therefore, we suggest that energy states in a material can be explored with the help of high excitation power which provides sufficient electrons.

To give a logical and reasonable explanation how the PL emission peak evolves, we propose a demonstration from the points of view both in the energy space and in the real space. There are two major groups of energy states in our system, including a higher-energy one (group A) and a lower-energy one (group B). Lower-energy states of group A come from the regions inside apertures while the SiO_2-capped regions outside apertures contribute to higher-energy states of group B. Density of states as a function of energy is schematically depicted in Fig. 3.16.

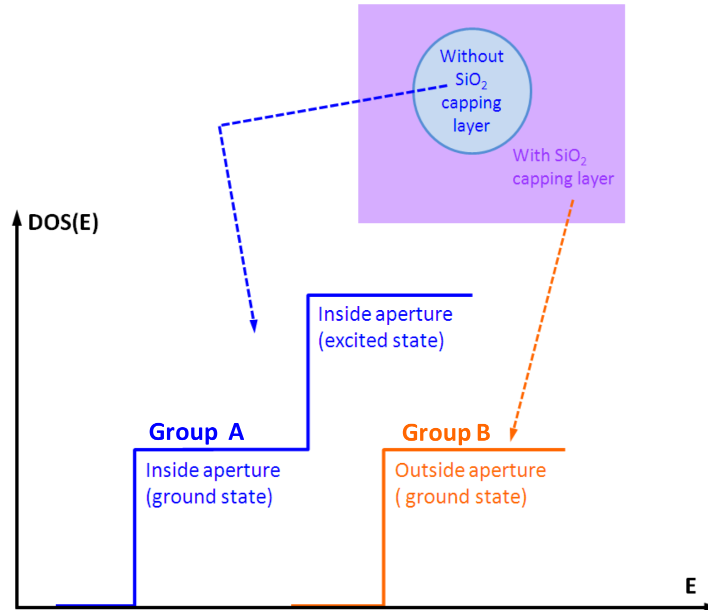

Fig. 3.16 Schematic of density of states (DOS). The blue line labeled as "Group A" corresponds to the regions inside apertures while the orange line labeled as "Group B" corresponds to the regions outside apertures. The area outside the apertures is covered with SiO_2 films.

Table 3.3 schematically demonstrates the gradual evolution of the transformation in the PL spectra. Electrons pumped to the $InGaAs/GaAs$ heterostructure are assumed to obey Fermi-Dirac distribution. In the first column, which is derived from the energy space, Fermi-Dirac distribution of electrons shows its position in relation to density of states and is presented as green dashed line. In the second column, which is derived from the real space, distribution of electrons is associated with excitation power density. Pumped electrons first fill in the lower-energy regions inside apertures, and then excess electrons, provided by increasing excitation power density, flow outward to the higher-energy regions capped with SiO_2 layer. Combining the phenomena occurred in the energy space and the real space, the corresponding micro-photoluminescence spectra are shown in the third column.

The photoluminescence spectra are classified into four stages illustrated in Table 3.3. As for stage (I), the excitation power is so low that only small part of ground states in group A is filled. In this case, all the pumped electrons are confined in the regions inside apertures. As a consequence, only one emission peak can be observed and the full with at half maximum (FWHM) is narrow.

In stage (II), more electrons allowed to occupy relatively higher-energy levels give the result that larger part of ground states in group A is filled. The pumped electrons occupying the relatively higher-energy ground states in group A lead to the non-uniform broadening, as known as Fermi-filling of the 2-D step-like DOS in quantum well systems.

When the excitation power of stage (III) is getting much higher, some electrons may fill in the excited states of group A and result in a shoulder-like side peak at around 1.401 eV. At the same time, few pumped electrons with even higher energy move towards the regions outside apertures which correspond to the ground states of group B. That is to say, the distribution of pumped electrons is expanding across the boundary of apertures. A higher-energy peak coming from group B turns out to appear at 1.450 eV.

In the final stage (IV), the ground states of group A are completely filled, and thus the PL intensity of the emission peak at 1.33 eV no longer increases. All of the excessively pumped electrons make contribution to magnifying the PL intensity of the excited states of group A and the ground states of group B. We can tell from the increase of the emission peak at 1.450 eV that the distribution of pumped electrons keeps expanding outwards and more regions outside apertures are covered. In the real space, the electron diffusion length in $GaAs$-based semiconductor materials can be several μm while both the size of diameter and periodicity is less than 1 μm. On this basis, the electrons pumped to the sample surface can move freely between group A (inside the apertures) and group B (outside the apertures) in the real space and perfectly follow the rules in the energy space.

Table. 3.3 Distribution of electrons and the corresponding PL spectrum

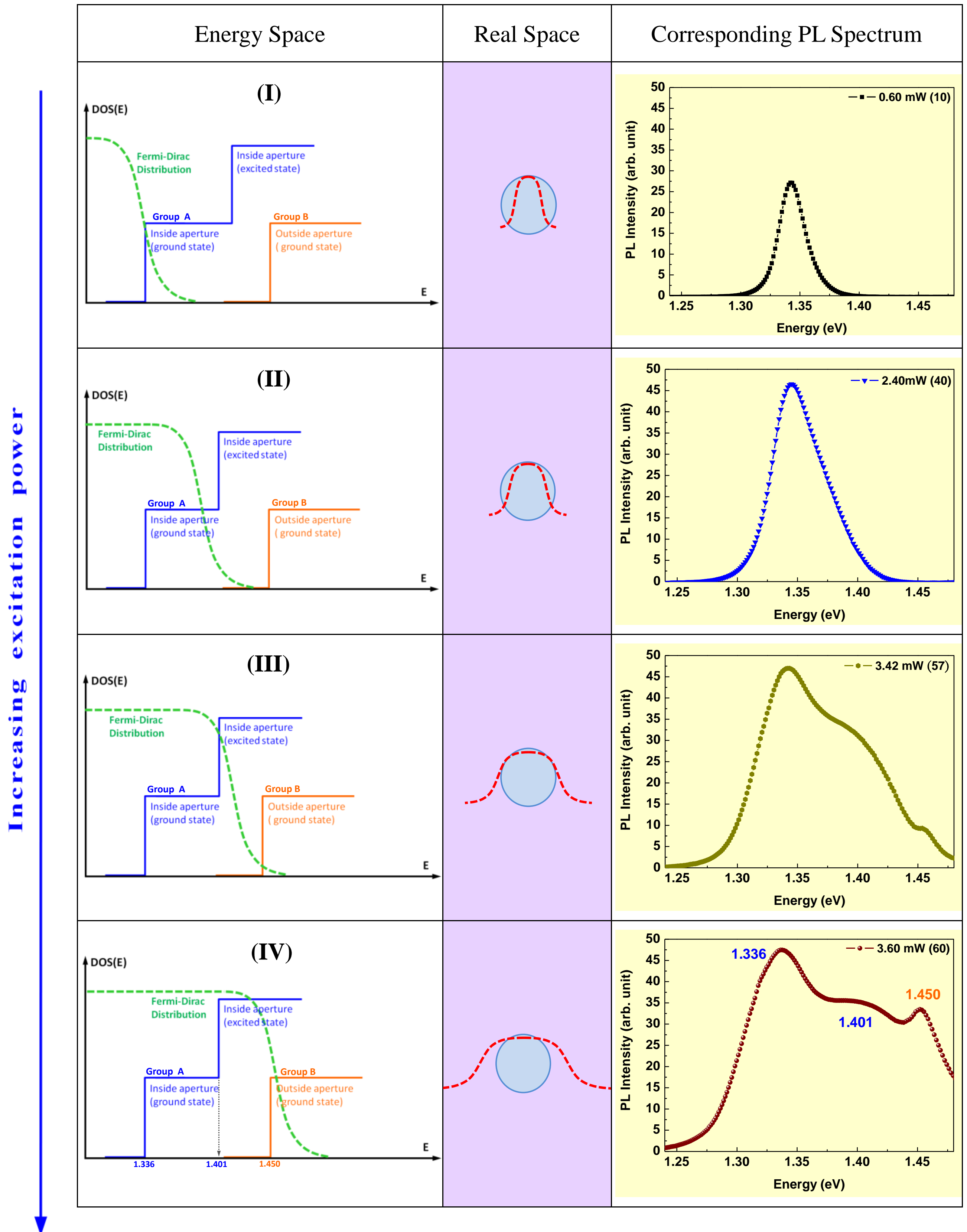

From the micro-PL spectrum of stage (IV), the main emission peaks from the regions inside and outside apertures were located at 1.336 eV and 1.450 eV respectively, and these two values served as the first eigen-energies for each case. The effective diffusion lengths (L_d) of Ga atoms were calculated by using COMSOL, a finite element analysis software, to solve $Schrödinger\ Equation$. The parameters were set to be $InGaAs_{as-grown} = In_{0.22}Ga_{0.78}As$, $E_{In_{0.22}Ga_{0.78}As}(77K) = 0.396\ eV$, $E_{GaAs}(77K) = 1.477\ eV$, $\frac{Conduction\ band\ offset}{Valence\ band\ offset} = \frac{60}{40}$, $w(\ well\ width\ of\ In_{0.22}Ga_{0.78}As) = 8\ nm$. The simulation results of wave function are shown in Fig. 3.17. Without the help of SiO_2 capping layer, the effective diffusion length was only 1.25 nm, and electrons and holes stayed close to the quantum well. It can be inferred that the degree of quantum well intermixing is slight in the regions uncapped with SiO_2 films. In the regions outside apertures, SiO_2 capping layer dramatically enhanced the quantum well intermixing and led to such a long diffusion length as 14.7 nm. Electrons and holes were no longer confined in the proximity of quantum well and diffused outwards to cover considerably large area.

In order to identify the positions of ground state and excited state in both the conduction band and the valence band, Fig. 3.18 shows the band structures plotted by MATLAB. The valence band structures were simulated for heavy holes (HH). The levels of ground state and first excited state are labeled with blue horizontal lines in the upper part of Fig. 3.18 (a) while only the ground state of valence band is shown in the lower part. Similarly, the levels of ground state in the conduction band and valence band are indicated with orange horizontal lines. The excited states were not taken into consideration in the case (b) representing the regions capped with SiO_2. The relation of density of states (DOS) between group A and B is clearly illustrated in Fig. 3.16 and further confirmed by the results of simulation.

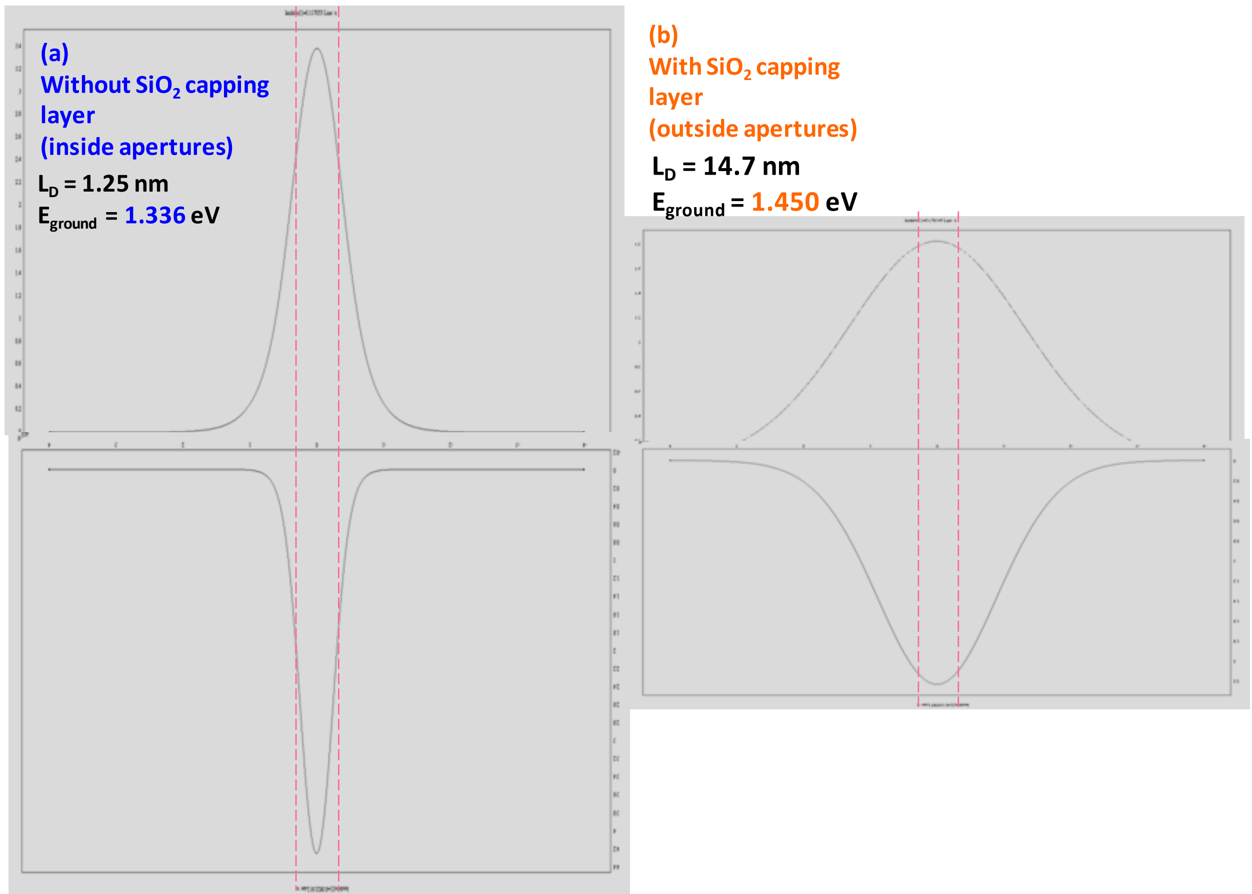

Fig. 3.17 Wave function distribution simulated by COMSOL. Red dashed lines indicate the position of $InGaAs$ quantum well which is 6 nm in width. The upper parts show the probability function of electrons in the conduction band, and the lower parts show the probability function of holes in the valence band. (a) In the regions inside apertures (without SiO_2 capping layer), the effective diffusion length of Ga atoms ($L_d = 1.25\ nm$) was deduced from $E_{ground} = 1.336\ eV$. (b) In the regions outside apertures (with SiO_2 capping layer), the effective diffusion length of Ga atoms ($L_d = 14.7\ nm$) was deduced from $E_{ground} = 1.450\ eV$.

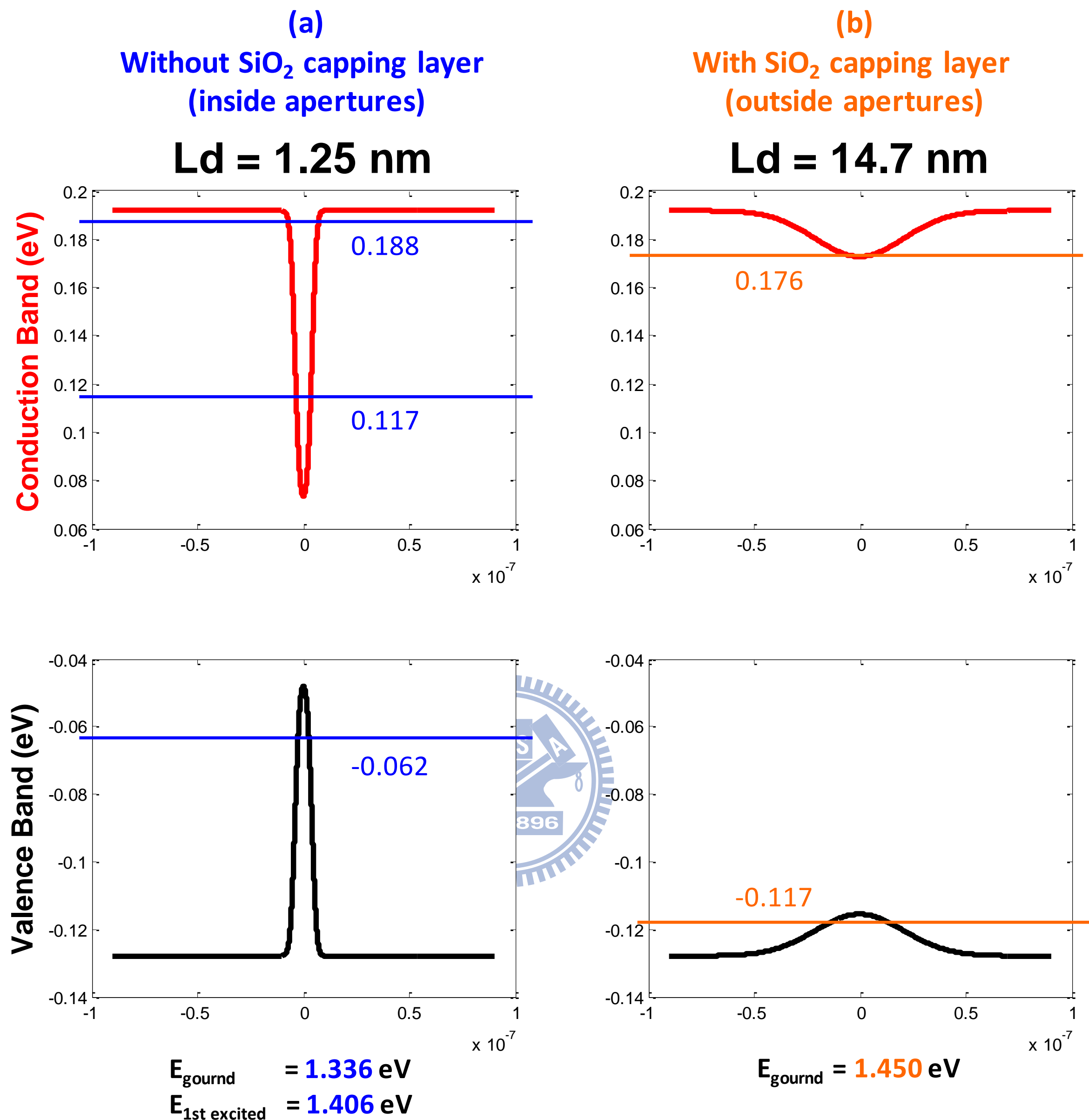

Fig. 3.18 Conduction band and valence band structures plotted by MATLAB. Conduction band structures are depicted with red lines in the upper diagrams. Valence band structures are depicted with black lines in the lower diagrams. The horizontal lines mark the levels of eigen-energies. (a) $L_d = 1.25\ nm$ represents the regions inside apertures (without SiO_2 capping layer). (b) $L_d = 14.7\ nm$ represents the regions outside apertures (with SiO_2 capping layer).

Chapter 4

Conclusions

We successfully demonstrated the temperature-dependent energy shifts induced by SiO_2 and TiO_2 capping layers. On the one hand, SiO_2-enhanced quantum well intermixing can be easily observed from the nearly exponential increase of energy shifts as the RTA temperature was used from 775 ℃ to 925 ℃. On the other hand, the samples capped with TiO_2 layer and annealed above 875 ℃ showed meaningful energy red-shifts and thus validated the ability of TiO_2 to inhibit quantum well intermixing.

The patterns with circular apertures which are sub-micrometer in diameter (d = 55, 75, 100, 125, 135 nm) were fabricated on the SiO_2 capping layers as masks. The aperture-dependent energy shifts from micro-photoluminescence spectra imply that the effective diameter of apertures is limited to a specific minimum value for each RTA temperature because lateral diffusion of Ga vacancies occurs simultaneously with the quantum well interdiffusion. In addition, we also explained the excitation power-dependent transformation of emission peaks from the points of view both in the real space and in the energy space.

Most important of all, we accomplished the selective area $InGaAs/GaAs$ quantum well intermixing on the sub-micrometer scale with the assistance of patterned SiO_2 capping layer.

Reference

[1] N. N. Ledentsov, *et al.*, "Quantum-dot heterostructure lasers," *Ieee Journal of Selected Topics in Quantum Electronics,* vol. 6, pp. 439-451, May-Jun 2000.

[2] V. M. Ustinov and A. E. Zhukov, "GaAs-based long-wavelength lasers," *Semiconductor Science and Technology,* vol. 15, pp. R41-R54, Aug 2000.

[3] A. D. Yoffe, "Semiconductor quantum dots and related systems: electronic, optical, luminescence and related properties of low dimensional systems," *Advances in Physics,* vol. 50, pp. 1-208, Jan 2001.

[4] J. H. Marsh, "Quantum-well intermixing," *Semiconductor Science and Technology,* vol. 8, pp. 1136-1155, Jun 1993.

[5] S. Mokkapati, *et al.*, "Controlling the properties of InGaAs quantum dots by selective-area epitaxy," *Applied Physics Letters,* vol. 86, p. 3, Mar 2005.

[6] J. Tatebayashi, *et al.*, "Area-controlled growth of InAs quantum dots and improvement of density and size distribution," *Applied Physics Letters,* vol. 77, pp. 3382-3384, Nov 2000.

[7] P. Lever, *et al.*, "Impurity free vacancy disordering of InGaAs quantum dots," *Journal of Applied Physics,* vol. 96, pp. 7544-7548, Dec 2004.

[8] Y. M. Park, *et al.*, "Interdiffusion and structural change in an InGaAs dots-in-a-well structure by rapid thermal annealing," *Journal of Applied Physics,* vol. 96, pp. 5496-5499, Nov 2004.

[9] D. G. Deppe and N. Holonyak, "Atom diffusion and impurity-induced layer disordering in quantum well III-V semiconductor heterostructues," *Journal of Applied Physics,* vol. 64, pp. R93-R113, Dec 1988.

[10] H. Leier, *et al.*, "Mass and dose dependence of ion-implantation-induced intermixing of GaAs/GaAlAs quantum-well structures," *Journal of Applied Physics,* vol. 67, pp. 1805-1813, Feb 1990.

[11] C. J. McLean, *et al.*, "Layer selective disordering by photoabsorption-induced thermal-diffusion in InGaAs/InP based multiquantum well structures," *Electronics Letters,* vol. 28, pp. 1117-1119, Jun 1992.

[12] J. J. Dubowski, *et al.*, "Laser-induced InAs/GaAs quantum dot intermixing," *Applied Physics Letters,* vol. 77, pp. 3583-3585, Nov 2000.

[13] P. Bhattacharya, *et al.*, "Quantum dot opto-electronic devices," *Annual Review of Materials Research,* vol. 34, pp. 1-40, 2004.

[14] S. Burkner, *et al.*, "Process parameter dependence of impurity-free interdiffusion GaAs/$Al_xGa_{1-x}As$ and $In_yGa_{1-y}As$/GaAs multiple-quantum wells," *Journal of Electronic Materials,* vol. 24, pp. 805-812, Jul 1995.

[15] A. S. W. Lee, *et al.*, "Comparison of quantum well intermixing in GaAs structures using a low temperature grown epitaxial layer or a SiO_2 cap," *Journal of Applied Physics,* vol. 100, Jul 2006.

[16] H. S. Lee, *et al.*, "Selective area wavelength tuning of InAs/GaAs quantum dots obtained by TiO_2 and SiO_2 layer patterning," *Applied Physics Letters,* vol. 94, p. 3, Apr 2009.

[17] L. Fu, *et al.*, "Suppression of interdiffusion in InGaAs/GaAs quantum dots using dielectric layer of titanium dioxide," *Applied Physics Letters,* vol. 82, pp. 2613-2615, Apr 2003.

[18] K. Kaviani, *et al.*, "Growth of high-quality strained $Al_xGa_{1-x}As/In_{0.26}Ga_{0.74}As/Al_zGa_{1-z}As$ quantum-wells and the effect of Silicon-Nitride encapsulation and rapid thermal annealing," *Journal of Vacuum Science & Technology B,* vol. 10, pp. 793-796, Mar-Apr 1992.

[19] J. F. Hazell, *et al.*, "Intermixing of InGaAsP/InGaAsP quantum-well structures using dielectric films," *Semiconductor Science and Technology,* vol. 16, pp. 986-991, Dec 2001.

[20] J. Beauvais, *et al.*, "Suppression of bandgap shifts in GaAs/AlGaAs quantu-wells using Strontium Fluoride caps," *Electronics Letters,* vol. 28, pp. 1670-1672, Aug 1992.

[21] P. N. K. Deenapanray and C. Jagadish, "Effect of stress on impurity-free quantum well intermixing," *Electrochemical and Solid State Letters,* vol. 4, pp. G11-G13, Feb 2001.

[22] J. S. Tsang, *et al.*, "Compositional disordering of InGaAs/GaAs heterostructures by low-temperature-grown GaAs layers," *Journal of Applied Physics,* vol. 79, pp. 664-670, Jan 1996.

[23] S. V. Zaitsev, *et al.*, "Production of quantum dots by selective interdiffusion in CdTe/CdMgTe quantum wells," *Semiconductors,* vol. 41, pp. 1339-1344, Nov 2007.

Appendix A

Epitaxy Structures

Layer	Thickness
SiO_2	150 nm
GaAs	10 nm
$Al_{0.4}GaAs$	30 nm
GaAs	6 nm
$In_{0.22}GaAs$	6 nm
GaAs	6 nm
$Al_{0.4}GaAs$	1 μm
Buffer GaAs	100 nm
GaAs	5 nm
AlAs	5 nm
GaAs S. I. Substrate	

Superlattice of 10-pair GaAs / AlAs

Fig. A.1 The schematic epitaxy structure of sample A which was designed for a $In_{0.22}Ga_{0.78}As/GaAs$ single quantum well. The capping layer of 150 nm SiO_2 film was deposited on the top of the semiconductor surface.

Layer	Thickness	
TiO_2	200 nm	
GaAs	10 nm	
$Al_{0.4}GaAs$	30 nm	
GaAs	6 nm	
$In_{0.27}GaAs$	3 nm	
GaAs	6 nm	
$Al_{0.4}GaAs$	1 μm	
GaAs	5 nm	Superlattice of 10-pair GaAs / AlAs
AlAs	5 nm	
Buffer GaAs	100 nm	
GaAs S. I. Substrate		

Fig. A.2 The schematic epitaxy structure of sample B which was designed for a $In_{0.27}Ga_{0.73}As/GaAs$ single quantum well. The capping layer of 200 nm TiO_2 film was deposited on the top of the semiconductor surface.

Appendix B

Experiment Techniques

Reactive Ion Etching

Table B.1 SiO_2 etching recipe

CHF_3 gas	25	sccm
Ar gas	25	sccm
RF power	200	Watts
Pressure	30	mTorr

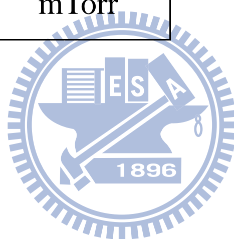

Rapid Thermal Annealing

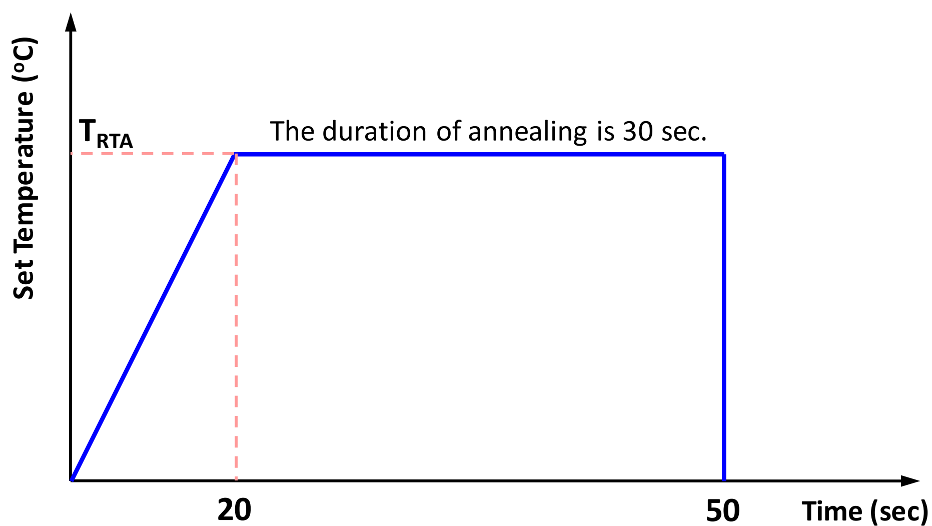

Fig. B.1 Rapid thermal annealing (RTA) recipe

Appendix C

Measurement Systems

Micro-Photoluminescence Setup

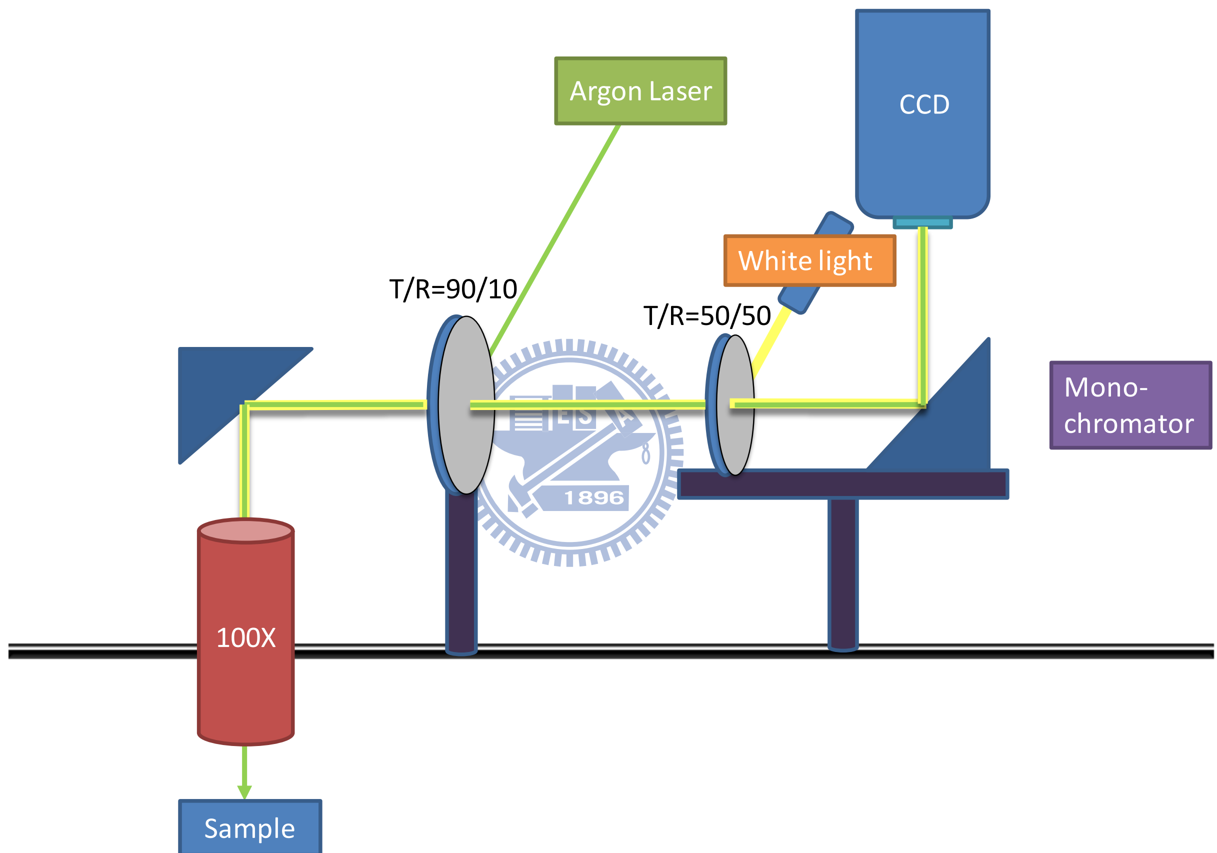

Fig. C.1 Schematic of micro-photoluminescence (micro-PL) measure system and the light path of image capturing.

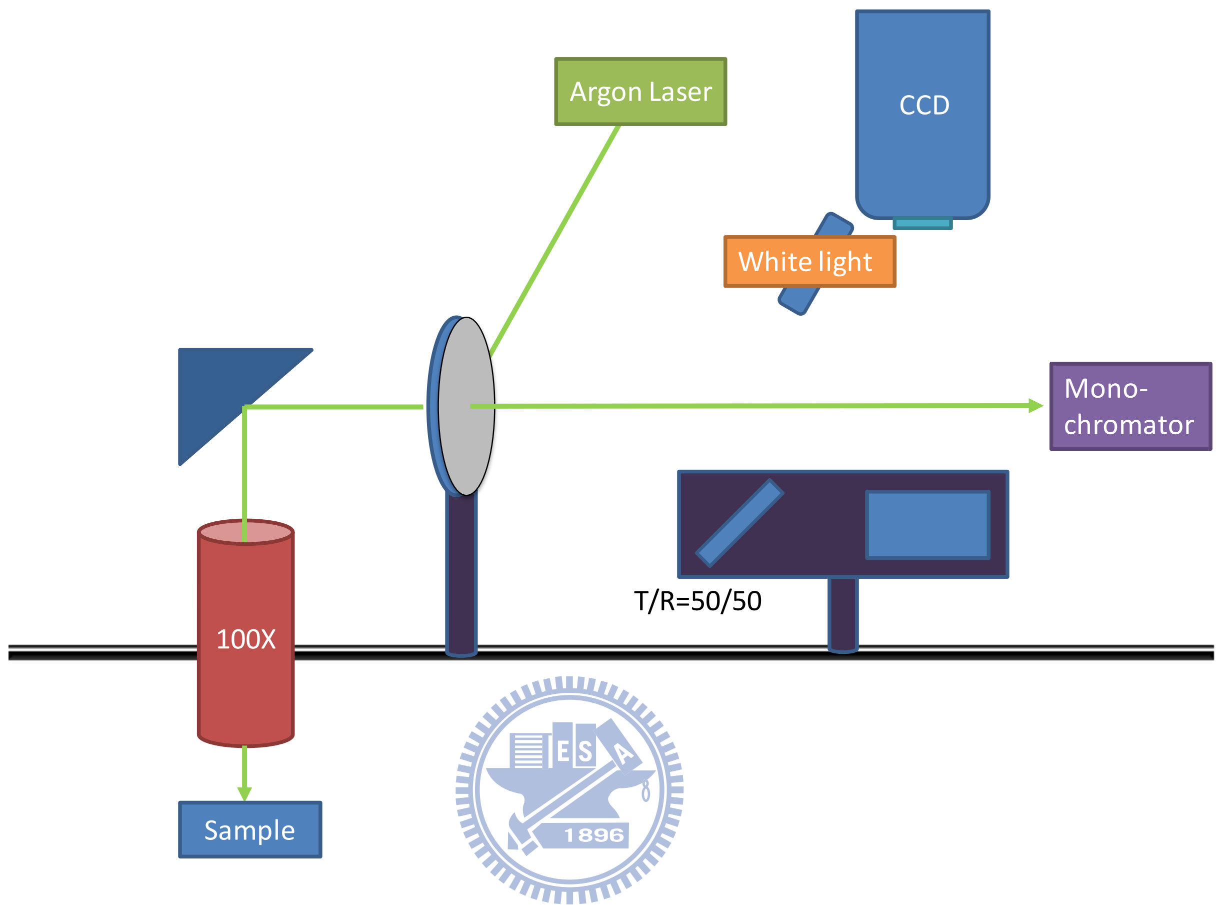

Fig. C.2 Schematic of micro-photoluminescence (micro-PL) measure system and the light path of spectra measuring.

Appendix D

Parameters and Equations

m_e	$(0.067 - 0.044\chi_i)m_0$	kg
m_h	$(0.45 - 0.1\chi_i)m_0$	kg
$D(T)$	$D_0 \cdot e^{\frac{-E_A}{k_B T}}$	$m^2/_s$
L_D	$\sqrt{Dt}$	m
χ_i	$\chi_i(x) = \frac{1}{2}\chi_o \left[erf\left(\frac{\frac{w}{2} - x}{2L_D}\right) + erf\left(\frac{\frac{w}{2} + x}{2L_D}\right) \right]$	
$CBO : VBO$	$CBO : VBO = 60 : 40$	
V_c	$V_c = CBO \times \Delta E$	eV
V_v	$V_v = VBO \times \Delta E$	eV
ΔE	$Eg_{In_{\chi_i}Ga_{(1-\chi_i)}As} - Eg_{In_{\chi_o}Ga_{\chi_o(1-\chi_o)}As}$	eV
ε	$\varepsilon = \frac{a_{sub} - a_{epi}}{a_{epi}} = \frac{a_{GaAs} - a_{InGaAs}}{a_{InGaAs}}$	
a_{GaAs}	5.6533	$\dot{A}$
$a_{In_{\chi_i}Ga_{(1-\chi_i)}As}$	$5.6533 + 0.4051\chi_i$	$\dot{A}$
S	$H(a) + \delta(b)$	eV
S_c	$H(a_c) = 2a_c \frac{C_{11} - C_{12}}{C_{11}} \cdot \varepsilon$	eV
S_v	$H(a_v) + \delta(b) = \left(2a_v \frac{C_{11} - C_{12}}{C_{11}} \pm b \frac{C_{11} + 2C_{12}}{C_{11}}\right) \cdot \varepsilon$ $\pm : for\ {}^{HH}_{LH}$	eV

a, a_c, a_v	$-9.77 + 3.77\chi_i$	eV
b	$-1.7 - 0.1\chi_i$	eV
C_{11}	$11.88 - 3.551\chi_i$	$\times 10^{11}\, {dyn}/{cm^2}$
C_{12}	$5.38 - 0.854\chi_i$	$\times 10^{11}\, {dyn}/{cm^2}$

Schrödinger equation applying to lattice-matched systems

$$\left(\frac{-\hbar^2}{2m^*}\frac{\partial^2}{\partial x^2} + V\right)\varphi = E\varphi$$

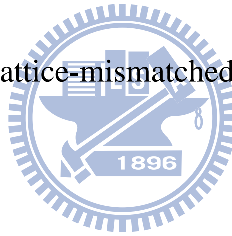

Schrödinger equation applying to lattice-mismatched systems

$$\left(\frac{-\hbar^2}{2m^*}\frac{\partial^2}{\partial x^2} + V + S\right)\varphi = E\varphi$$

Error function

$$\mathrm{erf}(x) = \frac{2}{\sqrt{\pi}}\int_0^x e^{-t^2}dt$$

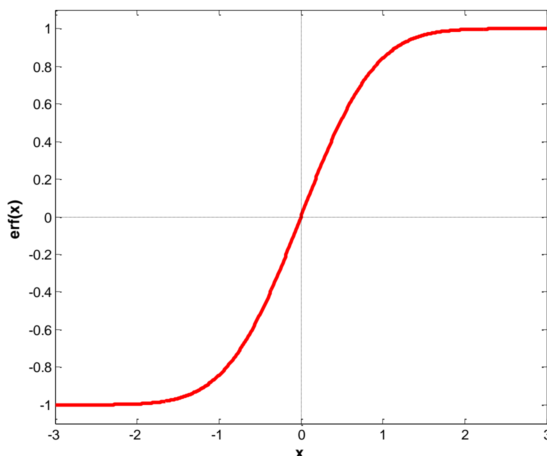

Vita

陳雅婷 **Atta Ya-Ting Chen**

EDUCATION

National Chiao Tung University, M. S., Dept. Electronics Engineering *Sep. 2008 – Jun. 2010*
National Taiwan University, B. S., Dept. Chemical Engineering *Sep. 2001 – Jun. 2005*
Taipei First Girls' High School *Sep. 1998 – Jun. 2001*

Work EXPERIENCE

Engineer,TFT Integration & Test Engineering Dept. *Feb. 2007 – Mar. 2008*
TFT Engineering / Manufacturing
AU Optronics Corporation, Central Taiwan Science Park

RESEARCH EXPERIENCE

Semiconductor Nanostructure & Quantum Device Laboratory **Advisor: Lee, Chien-Ping**
Department of Electronics Engineering, NCTU *Jul. 2008 – Jun. 2010*
Studies of SiO_2-Induced Selective Disordering of InGaAs/GaAs Quantum Wells

Impurity-free vacancy disordering (IFVD) has been regarded as one of the most promising post-regrowth bandgap tuning techniques which play an important role in the development of optoelectronic and photonic integrated applications. My study aimed at investigating the selective area quantum well intermixing induced by dielectric capping layers. The InGaAs/ GaAs quantum well heterostructures were capped with SiO_2 and TiO_2 films, and high-temperature rapid thermal annealing was applied subsequently. SiO_2-enhanced and TiO_2-inhibited quantum well intermixing respectively showed energy blue-shifts red-shifts in the micro-PL spectra. Furthermore, the patterns with circular apertures which are sub-micrometer in diameter were fabricated on the SiO_2 capping layers as masks. From the aperture-dependent micro-PL spectra, we suggest that the effective minimum diameter of apertures is limited to a specific value for each RTA temperature. We also demonstrated the distribution of electrons from the points of view both in the real space and in the energy space so as to explain the excitation power-dependent transformation of emission peaks. The selective area InGaAs/GaAs quantum well intermixing was accomplished on the sub-micrometer scale with the assistance of patterned SiO_2 capping layer. This controllable selective area quantum well intermixing on the sub-micrometer scale would pave a way to realize the monolithic integration of optoelectronic devices.

Biomolecular Engineering Laboratory **Advisor: Wang, Sheng-Shih**

Department of Chemical Engineering, NTU *Jun. 2004 – Jun. 2005*

The effects of small molecules on the aggregation of beta-amyloid and associated neurotoxicity in Alzheimer's disease

The formation and progressive deposition of beta-amyloid peptide (Aβ) is believed to be responsible for the neurodegeneration associated with Alzheimer's disease. To this end, we prepare Aβ peptide with various solvents, such as DMSO, TFA, and urea, in order to examine the molecular mechanism of Aβ aggregation. We also perform corresponding cell culture and biochemical analysis to better visualize the interaction between Aβ peptides. We expect to find small molecules and detergents that will provide sufficient intervention in the Aβ aggregation processes associated with neurotoxicity, and aid in the development of preventive strategies.

PERSONAL

Computer Skills: Microsoft Windows & Office, Matlab, Origin, AutoCAD, Comsol

Experimental Skills: DUV lithography, E-beam lithography, Wet bench, Inductively Coupled plasma reactive ion etch (ICP-RIE), E-gun deposition, Rapid thermal annealing (RTA), micro-photoluminescence (micro-PL), Scanning electron microscopy (SEM), Cell culture, Congo red binding analysis, SDS-PAGE of proteins